Complete Characterization of Optical Pulses in the Picosecond Regime for Ultrafast Communication Systems

by

Jade P. Wang

Submitted to the Department of Electrical Engineering and Computer Science in partial fulfillment of the requirements for the degree of

Master of Engineering in Electrical Engineering and Computer Science

at the

MASSACHUSETTS INSTITUTE OF TECHNOLOGY

August 2002

Author .....
Department of Electrical Engineering and Computer Science
August 21, 2002

Certified by .....
Erich P. Ippen
Elihu Thomson Professor of Electrical Engineering
Thesis Supervisor

Certified by .....
Scott A. Hamilton
MIT Lincoln Laboratory Staff Member
Thesis Supervisor

Accepted by .....
Arthur C. Smith
Chairman, Deparment Committee on Graduate Theses

Complete Characterization of Optical Pulses in the Picosecond Regime for Ultrafast Communication Systems

by

Jade P. Wang

Submitted to the Department of Electrical Engineering and Computer Science in partial fulfillment of the requirements for the degree of

Master of Engineering in Electrical Engineering and Computer Science

Abstract

Ultrashort optical pulses have a variety of applications, one of which is the development of optical time-devision multiplexing (OTDM) networks. Data is encoded in these short optical pulses (typically a few picoseconds in length) which are then interleaved in time to provide very high data rates on a single wavelength. Wavelength-division multiplexing (WDM) uses multiple channels by interleaving pulses in frequency in order to achieve high data rates. Typical pulse lengths in WDM are on the order of hundreds of picoseconds. OTDM networks have some advantages over WDM networks, but in order to take advantage of these characteristics, a better understanding of short optical pulse characterization needs to be reached. Such investigation requires accurate pulse characterization in the form of amplitude and phase measurements. Traditional methods of measurement such as nonlinear optical autocorrelation and spectral analysis cannot accurately measure pulse shape and phase. Two new methods of accurate characterization of amplitude and phase are frequency-resolved optical gating (FROG) developed by Rick Trebino, and a spectral interferometric method developed by Jean Debeau. The second-harmonic generation FROG method is highly sensitive but works best for femtosecond pulse lengths, due to the need for large spectrum. The spectral interferometric method is straightforward to implement using common fiber-coupled components, but suffers from a need for high pulse-to-pulse coherency, which implies that it is less practical for actual communication networks.

Thesis Supervisor: Erich P. Ippen
Title: Elihu Thomson Professor of Electrical Engineering
Thesis Supervisor: Scott A. Hamilton
Title: MIT Lincoln Laboratory Staff Member

Acknowledgments

First of all, I would like to thank my colleagues at the MIT Lincoln Laboratory, who have all been extremely patient and helpful in dealing with my many questions. My thesis advisor, Professor Erich Ippen, has been indispensable in helping me see this project to its end. Whenever some particularly recalcitrant problem has come up in the course of my experiments, he has always had the ability to see another path towards the eventual goal. My research supervisor, Dr. Scott Hamilton, always takes the time out to explain things thoroughly to me and taught me all the basics of working in a fiber optics lab. His guidance on this project has kept it alive far past the point when I would have been unable to proceed any further. Finally, his ability to successfully finish four things at once while still finding the time to help me with my work is very inspiring–and impressive.

Soon-to-be Dr. Bryan Robinson was also invaluable in his ability to mesh his practical knowledge of the laboratory with a sound mathematical and theoretical foundation. Without his help during the last few weeks, I could not have possibly finished this thesis. Shelby Savage, another student in the laboratory, was also extremely helpful in explaining difficult concepts in ways that I could understand. He would also often keep me sane during particularly frustrating bouts with the autocorrelator by providing a much-needed sense of humor. I would also like to thank Thomas Murphy, who was always happy to answer even the most trifling questions. I would also like to thank him particularly for putting up with me as an office mate. Steve Constantine has always encouraged me and made the impossible seem possible again. Todd Ulmer has always encouraged me by making me realize that things could always be worse. I would also like to thank Professor James K. Roberge, for showing me that I could do great things, and for believing in my abilities when I had doubts.

I would also like to thank my family and my friends from MIT and elsewhere, without whom I might have still finished this thesis but I certainly would not have finished it sane. My mother and father have always believed in my ability to finish what I begin, and to do it well. My brother has always been a source of encouragement to me, despite having grown apart these few years. I would like to thank my friends Keith Santarelli, for being an inspiration to me throughout my MIT career; Laura Kwinn and Sammi Truong for being able to put up with me as a roomate; Jennifer Chung, who is a great housemate and can always make me laugh; Edwin Karat, my generous housemate who had the dubious distinction of being pestered with a variety of technical questions and whose books were always extremely helpful; Emily Marcus, Laura Cerritelli, Susan Born, Jamie Morris, and Michelle Goldberg for always being ready to cheer me up; Karen Robinson and Juhi Chandalia for helping me through Nonlinear Optics and for the various fascinating conversations on our chosen field; Natalie Garner and Phil for showing me that there was more to life than nonlinear optics; and finally Jay Muchnij for being willing to listen to me past the point when any normal person would have fallen asleep. Finally, I would like to thank the denizens of the zephyr instance help, for their invaluable help in dealing with LaTeX.

Contents

Chapter 1

Introduction

Currently, there is a need, for a variety of applications, to create shorter and more precisely characterized optical pulses. Such pulses have large bandwidths, and thus are useful for material characterization via spectroscopy. Ultrashort pulses can be useful in imaging extremely fast temporal effects such as molecular rotations via "time strobing".[1] They are also useful in the field of medicine, whether in examining structures or performing surgery[2] without invading the body. For spectroscopic material characterization and temporal sampling, the optical pulsewidth is typically a few femtoseconds or less. Finally, short pulses are also necessary for the development of optical time-division multiplexing (OTDM) networks. In such networks, data is encoded in short optical pulses (typically a few picoseconds in length) which are then interleaved in time. This provides very high aggregate data rates in a single channel. Another method, wavelength-division multiplexing (WDM), interleaves pulse trains in frequency to achieve high data rates using multiple channels. The optical pulsewidths used in WDM systems today are typically hundreds of picoseconds long.

Recently, both OTDM and WDM fiber transmission links have been demonstrated at data rates exceeding one terabit/second.[3–5] Because such data rates are several orders of magnitude greater than electronic processing speeds, architecture for such systems must be carefully considered in order to implement extremely capable optical networks in the future. Most networks in use today are WDM networks, due to relative commercial component maturity, but OTDM networks have several potential advantages.[6] For instance, OTDM networks can simultaneously provide both guarenteed bandwidth and truly flexible bandwidth on demand service if slotted or packetized transmission is used. Network management and control are also easier to understand and to implement due to the single channel nature of the data. Furthermore, such networks are ideally suited to statistical multiplexing of data and much more scalable in the number of uses than WDM networks. However, in order to take advantage of these characteristics, several difficulties related to short optical pulse transmission need to be overcome. These difficulties include noise accumulation, the presence of group velocity dispersion (GVD), polarization-mode dispersion, and material nonlinearities. Investigation and ultimately control of these effects in ultrafast optical communication systems requires an accurate way of measuring short pulses that are a few picoseconds in length.

Traditional methods of measuring pulses include using the optical autocorrelation and the spectrum of the pulse in order to estimate the pulse width and shape. Optical autocorrelation is a technique in which the pulse under test is used to sample itself. However, due to the symmetric response, the autocorrelation is incapable of providing insight as to pulse envelope asymmetry or frequency chirping. Furthermore, the estimation of the pulse width is based upon an assumed pulse envelope shape, which may or may not be correct. Optical pulse characterization inferred from autocorrelation

measurements is not only inaccurate due to errors between the measured and assumed pulse shape, but incomplete because only temporal information is considered.

Complete characterization in the time or frequency domain requires both magnitude and phase (or temporal and spectral profile) of a pulse. With both temporal and spectral information, it is possible to determine the pulse characteristics completely, since spectral content is related to temporal content through the properties of the Fourier transform. However, in any measurement, we can only obtain temporal or spectral intensity of the signal. Pulse characterization is complicated further by the existence of chirp. The instantaneous frequency of a chirped pulse varies across the pulse, which means that the pulse is not transform-limited. Transform-limited pulses allow us to make assumptions about the relations between the spectral and temporal information of a pulse which can make characterization simpler.

There are several pulse characterization techniques which have been developed to completely determine pulse phase and magnitude. Interferometric techniques, which analyze the coherent interference between two copies of the pulse, are most effective in the nanosecond range. Another technique, called FROG (frequency-resolved optical gating), is aimed at femtosecond pulses with large bandwidths. For our systems, however, we need to characterize pulses in the picosecond regime. Picosecond pulses are particularly difficult to characterize, since they do not have the large bandwidth of femtosecond pulses, nor do they have the accessible temporal information of nanosecond pulses.

An interferometric method developed by Jean Debeau[7] has been demonstrated for picosecond pulse characterization. This method uses an electro-optic modulator to modulate the pulse train of interest at half the frequency of the pulse train. As

a result, the spectral lines of the pulse train of interest are mixed down and up into new spectral lines. Since each new spectral line contains information from exactly two adjacent original spectral lines, it is possible to extract the relative phases of the original spectral lines from the new spectral lines. Using picosecond width pulses at high repetition rates and a high-resolution spectrometer, it is possible to measure the phase of the pulses in the pulse train. This method uses common fiber-coupled equipment, making for a simple setup. Furthermore, it provides a method of measuring the phase profile of a pulse directly, without resorting to iterative algorithms. However, one large drawback which limits the generality of this method is the need for high pulse-to-pulse coherency in the pulse train of interest. This limits the generality of this method severely.

The frequency-resolved optical gating (FROG)[8–13] method relies upon simultaneously measuring the temporal and spectral pulse content, which is then displayed as a spectrogram. Using an iterative algorithm to characterize the measured spectrogram, we can then accurately determine the pulse amplitude, phase, and frequency chirp. Currently, a variety of FROG methods have been developed, including polarization-gate (PG) FROG, self-diffraction (SD) FROG, transient-grating (TG) FROG, second harmonic generation (SHG) FROG, and third harmonic generation (THG) FROG. Another method, the sonogram, involves finding the spectrogram in a way which is essentially the reverse of the FROG method.

Chapter 2 presents the theory behind pulse propagation in fibers, including dispersion, the nonlinear index of refraction, and the nonlinear Schrödinger equation. In preparation for later chapters, pulse distortion and its causes will also be discussed.

Chapter 3 will present the theory of frequency-resolved optical gating (FROG) and

its advantages and disadvantages for the picosecond regime. Simulations of FROG traces using second harmonic generation (SHG) FROG will be presented. Finally, we will close with a discussion on the algorithm for extracting the phase and amplitude of a pulse.

Chapter 4 will present the theory of interferometric pulse characterization and its advantages and disadvantages over the FROG method for the picosecond regime. Simulations of pulse characterization experiments will be presented for comparison with results shown in Chapter 5.

Chapter 5 will detail the experimental efforts in implementing a system which can completely characterize picosecond pulses. Results of the experiments will be analyzed and compared to simulations shown previously in Chapter 4.

Chapter 6 summarizes the conclusions of this thesis and provides suggestions for future work in this area.

Chapter 2

Pulse Propagation Theory

In fiber communication systems, short optical pulses are used to transmit data, with a variety of encoding schemes including return-to-zero (for OTDM) and non-return-to-zero (WDM). For simplicity, we consider an optical field as a superposition of monochromatic plane waves traveling in the z direction[14]

$$\mathbf{E}(z,t) = \sum_{\omega_a} \sum_{i=1}^{3} \hat{\mathbf{e}}_\mathbf{i} \frac{1}{2} \Big[E_i(\omega_a) e^{i(k_i z - \omega_a t)} + \text{c.c.} \Big]. \tag{2.1}$$

Here, the sum over ω_a sums over all frequencies. The second sum, over i, includes all three possible polarizations of the plane waves. We also define the intensity as the magnitude of the time averaged Poynting vector:

$$I(t) = \frac{nc\epsilon_o}{2} |E(t)|^2, \tag{2.2}$$

where we have dropped the spatial dependence for simplicity.

To generalize even further, we can assume quasi-monochromatic plane waves. For

this case, we can assume our electric field at a particular frequency ω can be written as a combination of a slowly-varying envelope ($A(\mathbf{r}, t)$) and a plane wave. This is a common representation for optical pulses as used in communication systems.

$$E(\omega_o, z, t) = \hat{e}A(\mathbf{r}, t)e^{i(kz-\omega_o t)}. \tag{2.3}$$

We drop the spatial dependence for simplicity and add a phase term,

$$E(\omega_o, t) = \hat{e}A(t)e^{-i(\omega_o t+\phi(t))}. \tag{2.4}$$

Instantaneous frequency is defined as

$$\omega_{\text{inst}} = \omega_o + \frac{d\phi(t)}{dt}. \tag{2.5}$$

For optical pulses, a useful term is chirp, which is defined as the second derivative of the phase of the pulse, or the first derivative of the instantaneous frequency.

$$\text{chirp} = \frac{d\omega_{\text{inst}}}{dt} = \frac{d^2\phi(t)}{dt^2}. \tag{2.6}$$

We can expand Equation (2.4)

$$E(\omega_o, t) = \hat{e}A(t)e^{-i(\omega_o t+C_o+C_1 t+C_2 t^2+C_3 t^3+...)}. \tag{2.7}$$

Here, we have explicitly written out the possible forms of the time-dependent phase. C_o and C_1 are coefficients for zero chirp. C_2 is the coefficient for constant chirp, C_3 is the coefficient for linearly time-varying chirp, and so on.

Chirp describes the variation of pulse phase across the length of the pulse itself.

When the pulse instantaneous frequency is constant, the pulse varies linearly with time and the pulse is described as having zero chirp. Constant chirp occurs when the pulse phase is quadratic and the pulse instantaneous frequency therefore varies linearly with time. Linear chirp occurs when the pulse phase is cubic and the instantaneous frequency is quadratic. Higher order instantaneous frequency dependence results in nonlinear chirp.

The presence of chirp in a pulse is typically induced both by dispersion and by nonlinearities in the medium through which the pulse propagates. nonlinearly induced chirp in a pulse increases its temporal broadening rate when the pulse propagates through a dispersive media. It can also cause a spectral broadening in the pulse without changing its intensity profile, thus causing problems for communications systems which rely on efficient use of bandwidth. Furthermore, without the ability to characterize the chirp of a pulse, it is much more difficult to predict how a given pulse will change envelope shape and width as it propagates. Figure 2.1 shows an example of a Gaussian pulse with constant chirp (quadratic phase) compared to an unchirped pulse. This comparison illustrates the effect of chirp on the bandwidth of a pulse.

Let us take a look at some common forms for the pulse envelopes ($A(t)$) as described in Equation (2.4)). A Gaussian envelope is of the form

$$E(t) = Be^{-\frac{t^2}{2\tau^2}}, \tag{2.8}$$

where B is a constant amplitude and τ is the half-width at the $1/e$ intensity point of the pulse. The more common measure of pulse width is the full-width at half-maximum (FWHM). Both τ and the FWHM are measured with regard to the intensity

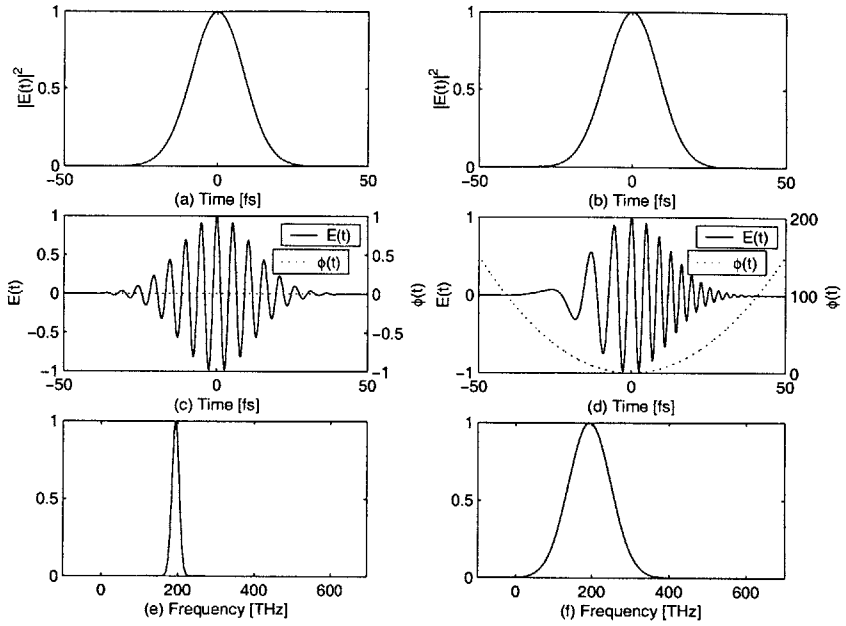

Figure 2.1: (a) and (b) show the intensity of the unchirped Gaussian and the chirped Gaussian, respectively. Note that they are identical. (c) shows the electric field of the unchirped Gaussian and the phase of the unchirped Gaussian. (d) shows the electric field and phase for a Gaussian of the same FWHM with constant chirp. (e) and (f) show the corresponding spectral intensities for the two Gaussians. For these plots, the FWHM is 20 fs. The quadratic chirp is 0.02 $[rad/fs^2]$. (fig/exgausschirps2.eps)

of the Gaussian pulse, given by

$$I(t) = I_o e^{-\frac{t^2}{\tau^2}}, \tag{2.9}$$

where $I_o = \frac{nc\epsilon}{2} B^2$. The FWHM is related to τ by the following relation

$$FWHM = 2\tau\sqrt{\ln 2}. \tag{2.10}$$

Gaussian pulses are common solutions to many laser outputs, including mode-locked

fiber lasers and diode lasers. A hyperbolic secant (sech) pulse envelope is the natural solution to the soliton equations. For more information on solitons, please refer to Chapter 5 of Agrawal.[15] Sech pulses take the form

$$E(t) = B\text{sech}\frac{t}{T_o}, \tag{2.11}$$

where B is the amplitude of the pulse, and T_o is related to the full-width at half maximum by

$$\text{FWHM} = 2T_o \ln(1+\sqrt{2}). \tag{2.12}$$

The full-width at half maximum is measured from the intensity envelope of the pulse. Figure 2.2 plots the intensities of a gaussian and a sech pulse, both with a full width at half maximum of 2 ps.

2.1 Nonlinear Polarization

Thus far, we have only considered electric fields in free space. Let us next consider how electromagnetic waves act within materials. We first consider a dielectric material. When an electric field is applied, the dielectric material polarizes and a polarization current is induced. This material polarization leads to a linear change in the index of refraction of the material as well as higher order nonlinear terms which act as new sources of electromagnetic radiation. The relation between the electric displacement $\mathbf{D}$, the electric field $\mathbf{E}$ and the electric polarization $\mathbf{P}$ is

$$\mathbf{D}(\mathbf{r},t) = \epsilon_o \mathbf{E}(\mathbf{r},t) + \mathbf{P}(\mathbf{r},t). \tag{2.13}$$

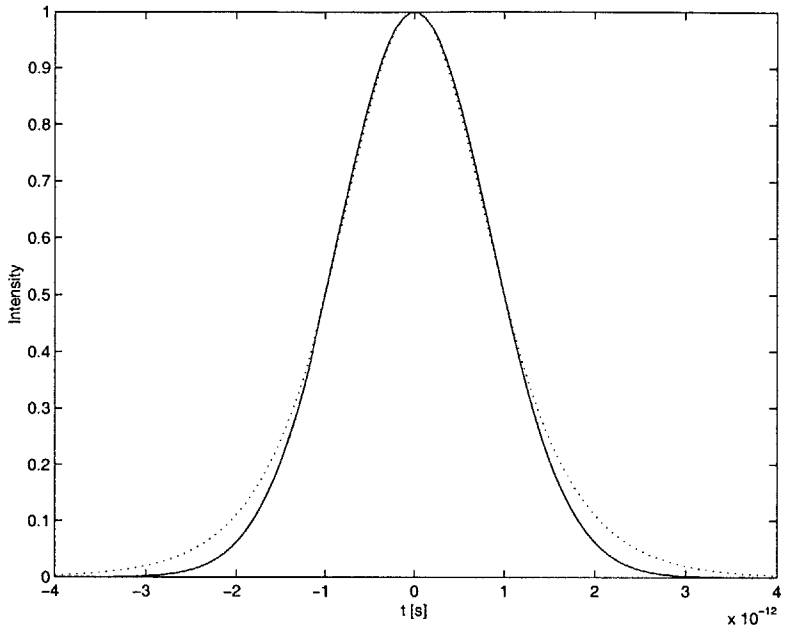

Figure 2.2: Example of an unchirped gaussian pulse with a full-width half-max of 2 ps (solid line) and unchirped sech pulse with same full-width half-max (dotted line). (fig/gausssech.eps)

The electric polarization of a dielectric material is defined to be the sum of the electric dipole moments per unit volume induced in the material by the presence of an electric field.[16] These electric dipole moments are induced over time scales defined by molecular, ionic, and electronic processes in the material. In silica fiber, the electronic effects dominate, which results in a nearly instantaneous response of approximately 10 fs.

The induced material polarization can be expanded into linear and nonlinear terms

$$\mathbf{P}(\mathbf{r},t) = \mathbf{P}^{L}(\mathbf{r},t) + \mathbf{P}^{NL}(\mathbf{r},t), \tag{2.14}$$

where

$$\mathbf{P}^{L}(\mathbf{r},t) = \mathbf{P}^{(1)}(\mathbf{r},t) \tag{2.15}$$

and

$$\mathbf{P}^{NL}(\mathbf{r},t) = \mathbf{P}^{(2)}(\mathbf{r},t) + \mathbf{P}^{(3)}(\mathbf{r},t) + \mathbf{P}^{(4)}(\mathbf{r},t) + ... \tag{2.16}$$

Using Fourier analysis, we can expand the polarization in an infinite sum of separate frequency components, similar to our earlier treatment of the electric field in Equation (2.1).

$$\mathbf{P}^{(n)}(\mathbf{r},t) = \sum_{\omega_b}\sum_{i}\hat{\mathbf{p}}_{\mathbf{i}}\frac{1}{2}\left[\mathbf{P}^{(n)}(\mathbf{r},\omega_b)e^{i(\mathbf{k_b}\cdot\mathbf{r}-\omega_b t)} + \text{c.c.}\right]. \tag{2.17}$$

Again, we first sum over frequencies and then sum over all possible polarizations. An example of a polarization $\mathbf{P}^{(n)}(\mathbf{r},\omega_m)$, for the case when only sum frequencies are included, is

$$\begin{aligned}\mathbf{P}(\mathbf{r},\omega_m) &= \epsilon_o(\chi^{(1)}(\omega_m=\omega_1)\cdot\mathbf{E}(\omega_1) + \chi^{(2)}(\omega_m=\omega_1+\omega_2):\mathbf{E}(\omega_1)\mathbf{E}(\omega_2) \\ &\quad + \chi^{(3)}(\omega_m=\omega_1+\omega_2+\omega_3)\vdots\mathbf{E}(\omega_1)\mathbf{E}(\omega_2)\mathbf{E}(\omega_3) + ...) \\ &= \mathbf{P}^{(1)}(\mathbf{r},\omega_m) + \mathbf{P}^{(2)}(\mathbf{r},\omega_m) + \mathbf{P}^{(3)}(\mathbf{r},\omega_m) + ...,\end{aligned} \tag{2.18}$$

where the χ's are the nonlinear susceptibilities. As a result of the vector nature of the electric field and polarization, the susceptibility is a tensor quality. The susceptibility of order n for nth order polarization and field is a tensor of order $n+1$. To illustrate the tensor nature of this term, we can explicity write out the third-order material

polarization in terms of the electric field and susceptibility:

$$\begin{bmatrix} P_x^{(3)}(\omega) \\ P_y^{(3)}(\omega) \\ P_z^{(3)}(\omega) \end{bmatrix} = \epsilon_o \begin{bmatrix} \chi_{xxxx}^{(3)} & \chi_{xxxy}^{(3)} & \cdots & \chi_{xzzz} \\ \chi_{yxxx}^{(3)} & \chi_{yxxy}^{(3)} & \cdots & \chi_{yzzz} \\ \chi_{zxxx}^{(3)} & \chi_{zxxy}^{(3)} & \cdots & \chi_{zzzz} \end{bmatrix} \begin{bmatrix} E_x(\omega_1) & E_x(\omega_2) & E_x(\omega_3) \\ E_x(\omega_1) & E_x(\omega_2) & E_y(\omega_3) \\ E_x(\omega_1) & E_x(\omega_2) & E_z(\omega_3) \\ E_x(\omega_1) & E_y(\omega_2) & E_x(\omega_3) \\ & \cdots & \\ & \cdots & \\ E_z(\omega_1) & E_z(\omega_2) & E_y(\omega_3) \\ E_z(\omega_1) & E_z(\omega_2) & E_z(\omega_3) \end{bmatrix} \tag{2.19}$$

It is clear that the χ tensor is a fourth-order tensor. We can also write this in a summation form as follows:

$$P_i^{(3)}(\omega = \omega_o + \omega_n + \omega_m) = \epsilon_o \sum_{jkl} \sum_{(mno)} \chi_{ijkl}^{(3)}(\omega = \omega_o + \omega_n + \omega_m : \omega_o, \omega_n, \omega_m) E_j(\omega_o) E_k(\omega_n) E_l(\omega_m). \tag{2.20}$$

We include the second summation, over (mno) to illustrate that the material polarization at a frequency ω only requires the frequency components of the relevant electric fields to sum up to ω. Thus, m,n,and o may take on any number as long as their sum gives us the correct frequency component for the material polarization. In general, the calculation of the material polarization is greatly simplified by the fact that due to symmetry conditions in many materials, many of the quantities in the χ tensors are zero.

In fiber, the second order susceptibility is negligible due to the symmetries of silica glass. As a result, fiber nonlinearities are mainly due to third order effects. Let us

consider the third order polarization, for an incident electric field with three frequency components. In a more general case when an optical pulse is considered, the incident electric field often consists of many more frequency components. We assume that each of the electric field components are polarized in the same direction and drop the space dependence in the following equations for simplicity. From Equation (2.1), we obtain

$$E(\omega) = \frac{1}{2}\Big(E(\omega_1)e^{-i\omega_1 t} + E(\omega_2)e^{-i\omega_2 t} + E(\omega_3)e^{-i\omega_3 t} + c.c.\Big). \tag{2.21}$$

The frequencies present in the material polarization will be third-order combinations of the frequencies present in the electric field. Thus, if we calculate $E(t)^3$, we can observe which frequencies will be present in the material polarization.

$$\begin{aligned} E(\omega)^3 &= \frac{1}{8}\Big(E(\omega_1)e^{-i\omega_1 t} + E(\omega_2)e^{-i\omega_2 t} + E(\omega_3)e^{-i\omega_3 t} + c.c.\Big)^3 \qquad (2.22)\\ &= \frac{1}{8}\Big(E(\omega_1)^3 e^{-3i\omega_1 t} + E(\omega_1)^2 E^*(\omega_1)e^{-i\omega_1 t} + 2E(\omega_1)E(\omega_2)E^*(\omega_3)e^{-i(\omega_1+\omega_2-omega_3)t} + ...\Big) \end{aligned}$$

From this, we see that all sum and difference combinations of its frequencies ω_1,$omega_2$, and ω_3 are possible. We can write the polarization in terms of its separate frequencies by looking at the Fourier transform. Thus, each frequency of the polarization corresponds to some combination of the incident E fields. There are 44 separate frequency components, the Fourier transform sum of these 44 separate components results in the total polarization. A few of the specific frequency components are written out

below.

$$P(\omega_1) = \frac{1}{4}\chi^{(3)}(3E(\omega_1)E^*(\omega_1) + 6E(\omega_2)E^*(\omega_2) + 6E(\omega_3)E^*(\omega_3))E(\omega_1) \quad (2.23)$$

$$P(3\omega_1) = \frac{1}{4}\chi^{(3)}E^3(\omega_1) \quad (2.24)$$

$$P(\omega_1 + \omega_2 + \omega_3) = \frac{6}{4}\chi^{(3)}E(\omega_1)E(\omega_2)E(\omega_3) \quad (2.25)$$

$$P(2\omega_2 - \omega_1) = \frac{3}{4}\chi^{(3)}E(\omega_2)^2E^*(\omega_1) \quad (2.26)$$

A more complete listing can be found in Boyd[17] (Boyd uses a slightly different notation).

The various contributions to the nonlinear polarizations are results of particular nonlinear processes. For example, second harmonic generation and sum harmonic generation are generated by second order $\chi^{(2)}$ nonlinearity, while self- and cross-phase modulation, four-wave mixing, and Raman scattering are examples of third order $\chi^{(3)}$ nonlinearity. Observable electric fields are always real and thus have both positive and negative frequencies associated with them. Mixtures of negative and positive frequencies in the mathematics help explain nonlinear phenomena such as the optical Kerr effect, optical rectification, and coherent anti-Stokes Raman scattering.

2.1.1 Intensity Dependent Index of Refraction

The material polarization as described above can cause nonlinear effects, especially in isotropic materials such as silica glass, where third-order effects dominate. One such effect is the intensity dependent index of refraction which can often cause distortions in optical pulses as they propagate through fiber. The intensity dependent index of refraction can be caused by either self-phase modulation (SPM) or cross-phase

modulation(XPM). In self-phase modulation, a pulse propagating in fiber induces an intensity-dependent nonlinear change in the index of refraction of the fiber. In cross-phase modulation, a second field causes an intensity-dependent nonlinear index of refraction experienced by the first field. These effects result from third order processes which are dominant in fiber since silica glass is isotropic. Thus, for fiber, we can write

$$\mathbf{D}(\omega) = \epsilon_o\Big(1 + \chi^{(1)}(\omega)\Big)\mathbf{E}(\omega) + \mathbf{P}^{(3)}(\omega), \tag{2.27}$$

where $P^{(3)}(\omega)$ can be expanded in the same way as in Equation 2.20. The index of refraction in the absence of nonlinear polarization is defined to be

$$n_o = \sqrt{1 + \chi^{(1)}(\omega)}. \tag{2.28}$$

Let us first consider the case of self-phase modulation in fiber. We assume an incident electric field at a single frequency ω

$$\mathbf{E}(\omega) = \frac{1}{2}\hat{x}(E_1(\omega)e^{-i\omega t} + E_1^*(\omega)e^{i\omega t}). \tag{2.29}$$

As stated before, self-phase modulation will cause a change in the index of refraction observed by the electric field. We define a new index of refraction as

$$n = n_o + \Delta n, \tag{2.30}$$

where Δn is the change caused by SPM. To solve for Δn, we consider the nonlinear polarization in Equation (2.27). For self-phase modulation, the relevant third-order material polarization term is that which occurs at the same frequency as the incident

field and with the same polarization.

$$P_x^{(3)}(\omega) = \frac{\epsilon_o}{4}\{\chi^{(3)}_{xxxx}(\omega:\omega,\omega,-\omega)E_1(\omega)E_1(\omega)E_1^*(-\omega) + \chi^{(3)}_{xxxx}(\omega:\omega,-\omega,\omega)E_1(\omega)E_1^*(-\omega)E_1(\omega) + \chi^{(3)}_{xxxx}(\omega:-\omega,\omega,\omega)E_1^*(-\omega)E_1(\omega)E_1(\omega)\}. \tag{2.31}$$

Due to intrinsic permutation symmetry, we can interchange the frequency arguments at the same time we interchange the cartesian indices. In our case, the cartesian indices are all the same. As a result, we can sum all three terms, which gives us a coefficient of 3. Rewriting Equation (2.27) for self-phase modulation in fiber we obtain

$$D_x(\omega) = \epsilon_o(1+\chi^{(1)}_{xx}(\omega))E_1(\omega) + \frac{3\epsilon_o}{4}\chi^{(3)}_{xxxx}(\omega)|E_1(\omega)|^2E_1(\omega). \tag{2.32}$$

We can rewrite Equation (2.32)

$$D_x(\omega) = \epsilon_o(1+\chi^{(1)}_{xx}(\omega) + \frac{3}{4}\chi^{(3)}_{xxxx}(\omega)|E_1(\omega)|^2)E_1(\omega). \tag{2.33}$$

Using Equations (2.28), (2.30) and (2.32), we can see that

$$n^2 = (n_o+\Delta n)^2 = \big(1+\chi^{(1)}_{xx}(\omega) + \frac{3}{4}\chi^{(3)}_{xxxx}(\omega)|E_1(\omega)|^2\big). \tag{2.34}$$

We find that the change in the index of refraction is both nonlinear and proportional to the intensity of the field. Let us define Δn to be $n_2 I$, where n_2 is a constant of proportionality. Thus, Equation (2.30) becomes

$$n = n_o + n_2 I, \tag{2.35}$$

where I is defined (from Equation (2.2)) as

$$I = \frac{n_o \epsilon_o c}{2} c|E_1(\omega)|^2. \tag{2.36}$$

We now solve for n_2. Substituting Equation (2.35) into Equation (2.34), we obtain

$$(n_o^2 + 2n_o n_2 I + n_2^2 I^2) = 1 + \chi^{(1)}(\omega) + \frac{3}{4}\chi^{(3)}_{xxxx}(\omega)|E_1(\omega)|^2. \tag{2.37}$$

Since n_2 is typically very small, $n_2^2 I^2$ is negligible and can be neglected. Furthermore, we can also cancel out several terms by substituting in Equation (2.28), finally obtaining

$$2n_o n_2 I = \frac{3}{4}\chi^{(3)}_{xxxx}(\omega)|E_1(\omega)|^2. \tag{2.38}$$

Substituting Equation (2.36) into Equation (2.38) and solving for n_2, we obtain

$$n_2 = \frac{3}{4}\frac{1}{\epsilon_o n_o^2 c}\chi^{(3)}_{xxxx}(\omega). \tag{2.39}$$

We see from Equation (2.39) that self-phase modulation causes a change in the index of refraction proportional to the intensity of the field. This implies that an intensity-dependent phase shift will be induced upon the field. In the case of propagating pulses, the phase shift induced upon the pulse is dependent on the pulse intensity, which varies across the pulse envelope. In other words, the pulse will acquire increased bandwidth as well as chirp as it propagates.

The derivation of self-phase modulation derived here was for a linearly-polarized field. For a circularly polarized field, the constant of proportionality n_2 is $\frac{2}{3}$ that for a linearly polarized field. To gain a better understanding of the intensity-dependent

index of refraction, let us briefly consider n_2 for cross-phase modulation. In cross-phase modulation, a strong field (pump) can affect the index of refraction seen by a second, weaker field (probe) in much the same way as a field can affect itself in SPM. In order to calculate n_2 for a XPM effect, we must first realize that there are several different types of cross-phase modulation.

1. The pump is of the same polarization as the probe, but of different frequency.
2. The pump is of different polarization than the probe, but is of the same frequency.
3. The pump is of the same polarization and same frequency as the probe, but is sent in at a different angle from the probe to distiguish the two fields from each other.
4. The pump and probe are circularly polarized instead of linearly polarized.

Let us consider cross-phase modulation in the case where the pump and probe have the same (linear) polarization but different frequencies. We assume a pump field

$$\mathbf{E}_1 = \frac{1}{2}\hat{x}(E_1 e^{-i\omega_1 t} + E_1^* e^{i\omega_1 t}), \tag{2.40}$$

and a probe field

$$\mathbf{E}_2 = \frac{1}{2}\hat{x}(E_2 e^{-i\omega_2 t} + E_2^* e^{i\omega_2 t}). \tag{2.41}$$

For simplicity, we shall drop the vector notations. Again, assuming intrinsic permutation symmetry, the relevant third-order polarization term for cross-phase modulation

is

$$P^3(\omega_2) = \frac{6\epsilon_o}{4}\chi^{(3)}(\omega_2 : \omega_1, -\omega_1, \omega_2)|E_1|^2 E_2. \tag{2.42}$$

Note that the two distinct pump and probe frequencies result in twice as many degenerate terms for XPM as compared to SPM in Equation (2.31). Repeating the same calculations as before, we find that n_2 for cross-phase modulation is twice that for self-phase modulation

$$n_2 = \frac{3}{2}\frac{1}{\epsilon_o n_o^2 c}\chi^{(3)}(\omega_2). \tag{2.43}$$

Let us take a closer look at how self-phase and cross-phase modulation may affect a pulse as it propagates through fiber. The propagation of a pulse in free space is determined by the propagation constant, $\mathbf{k}$, which is defined as

$$\mathbf{k} = \frac{\omega}{c}n. \tag{2.44}$$

This propagation constant is a vector. Within fiber, the propagating mode may still be characterized by a single propagation constant

$$\beta = \frac{\omega}{c}n_{eff}, \tag{2.45}$$

where n_{eff} is the effective index of refraction of the mode. However, the electric field strength varies with the transverse position as shown in Figure 2.3.

We have shown that a pulse propagating as a plane wave will undergo self-phase modulation, such that the index of refraction it sees is really the linear index n_o plus

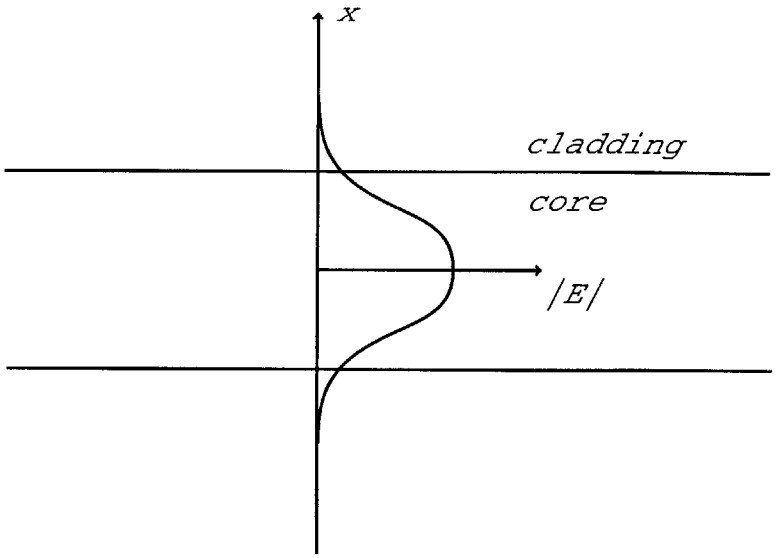

Figure 2.3: Electric field distribution in the lowest order fiber mode.
(fig/fiberbeta.eps)

some small intensity-dependent effect

$$n = n_o + n_2 I. \tag{2.46}$$

In a fiber, we find that the propagation constant is also altered by a small, intensity-dependent amount:

$$\beta = \frac{\omega}{c}(n_{eff} + n_{2_{eff}} I_p) = \beta_o + \Delta\beta, \tag{2.47}$$

where I_p is the peak intensity at the center of the guide and $n_{2_{eff}} = \int_\infty^\infty n_2 \frac{I(x)}{I_p} dx$ We find that $\Delta\beta$ is therefore

$$\Delta\beta = \frac{\omega}{c} n_{2_{eff}} I_p. \tag{2.48}$$

2.2 Wave propagation in Fibers

Now that we have gained some understanding in how electromagnetic waves behave in dielectric materials and how that might effect the propagation of these waves in a fiber medium, let us take a look at electromagnetic waves propagation in fiber. We begin with Maxwell's equations, which state

$$\nabla \times \mathbf{E} = -\frac{\partial \mathbf{B}}{\partial t} \tag{2.49}$$

$$\nabla \times \mathbf{H} = \frac{\partial \mathbf{D}}{\partial t} + \mathbf{J} \tag{2.50}$$

$$\nabla \cdot \mathbf{D} = \rho \tag{2.51}$$

$$\nabla \cdot \mathbf{B} = 0 \tag{2.52}$$

With continuity equations

$$\mathbf{B} = \mu \mathbf{H} \tag{2.53}$$

$$\mathbf{D} = \epsilon_o \mathbf{E} + \mathbf{P} \tag{2.54}$$

$$\mathbf{J} = \sigma \mathbf{E}. \tag{2.55}$$

We assume the material is nonmagnetic, so μ becomes the constant μ_o. We also assume that we are in a charge-free region, and thus ρ and $\mathbf{J}$ are both zero. Each of these assumptions makes sense because we are examining pulse propagation in optical fiber, which is a purely dielectric waveguide. To derive the wave equation, we take the curl of Equation (2.49) , and substitute in Equation (2.50):

$$\nabla \times \nabla \times \mathbf{E} = -\mu_o \frac{\partial^2 \mathbf{D}}{\partial t^2}. \tag{2.56}$$

Substituting in Equation (2.54) gives us

$$\nabla \times \nabla \times \mathbf{E} = -\mu_o \epsilon_o \frac{\partial^2 \mathbf{E}}{\partial t^2} - \mu_o \frac{\partial^2 \mathbf{P}}{\partial t^2}. \tag{2.57}$$

If we then use the Fourier transform and analyze this equation in the frequency domain, we can simplify Equation (2.57) using the the simple relation between $\mathbf{E}$ and $\mathbf{P}$

$$\mathbf{P} = \epsilon_o(\chi^{(1)}\mathbf{E} + \chi^{(2)}\mathbf{E}\mathbf{E} + ...) = \mathbf{P}^L + \mathbf{P}^{NL}. \tag{2.58}$$

Since

$$\mathbf{P}^L = \epsilon_o \chi^{(1)}\mathbf{E}, \tag{2.59}$$

we can define $\epsilon = \epsilon_o(1 + \chi^{(1)})$. Using Equations (2.58) and (2.59) and assuming an instantaneous material susceptibility $\chi^{(1)}$, Equation (2.57) becomes:

$$\nabla \times \nabla \times \mathbf{E} + \mu_o \epsilon \cdot \frac{\partial^2 \mathbf{E}}{\partial t^2} = -\mu_o \frac{\partial^2 \mathbf{P}^{NL}}{\partial t^2}. \tag{2.60}$$

We can further simplify Equation (2.60) by using the following vector identity and realizing

$$\nabla \times \nabla \times \mathbf{E} = \nabla(\nabla \cdot \mathbf{E}) - \nabla^2 \mathbf{E} \approx -\nabla^2 \mathbf{E}. \tag{2.61}$$

Now, since the term $\nabla \cdot \mathbf{E}$ tends to be very small for slowly varying amplitudes and plane waves, even in nonlinear systems, then the final equation is

$$\nabla^2 \mathbf{E} - \mu_o \epsilon \cdot \frac{\partial^2 \mathbf{E}}{\partial t^2} = \mu_o \frac{\partial^2 \mathbf{P}^{NL}}{\partial t^2}. \tag{2.62}$$

Equation (2.62) is called the nonlinear wave equation and has the form of an inhomogenous Helmholtz equation.

We proceed to simplify this equation assuming plane wave propagation with a slowly-varying envelope at frequency ω

$$\mathbf{E}(z, \omega, t) = \hat{\mathbf{e}} E(z, t) e^{-i(\omega t - kz)}, \tag{2.63}$$

where $E(z, t)$ is a slowly-varying envelope and $e^{-i(\omega t - kz)}$ is the monochromatic plane wave. We also assume that the material polarization is of the same form

$$\mathbf{P}^{NL}(z, \omega, t) = \hat{\mathbf{p}} P^{NL}(z, t) e^{-i(\omega t - k_p z)}, \tag{2.64}$$

where the wave number for the nonlinear polarization component k_p is distinct from the electric field wave number k in order to account for the phase mismatch between each wave. To simplify Equation (2.62), we need to substitute in Equations (2.63) and (2.64). We take some derivatives first in order to make the substitution process

easier.

$$\frac{\partial E(z,\omega,t)}{\partial t} = \hat{e}\Big(\frac{\partial}{\partial t} - i\omega\Big)E(z,t)e^{-i(\omega t - kz)} \tag{2.65}$$

$$\frac{\partial^2 E(z,\omega,t)}{\partial t^2} = \hat{e}\Big(\frac{\partial^2}{\partial t^2} - 2i\omega\frac{\partial}{\partial t} - \omega^2\Big)E(z,t)e^{-i(\omega t - kz)} \tag{2.66}$$

$$\frac{\partial E(z,\omega,t)}{\partial z} = \hat{e}\Big(\frac{\partial}{\partial z} + ik\Big)E(z,t)e^{-i(\omega t - kz)} \tag{2.67}$$

$$\frac{\partial^2 E(z,\omega,t)}{\partial z^2} = \hat{e}\Big(\frac{\partial^2}{\partial z^2} + 2ik\frac{\partial}{\partial z} - k^2\Big)E(z,t)e^{-i(\omega t - kz)}. \tag{2.68}$$

The derivatives for $P^{NL}(z,\omega,t)$ are similar.

Using these derivatives to simplify Equation (2.62), we obtain

$$\hat{e}\Big\{\Big(\frac{\partial^2}{\partial z^2} + 2ik\frac{\partial}{\partial z} - k^2\Big) - \mu_o\epsilon(\omega)\Big(\frac{\partial^2}{\partial t^2} - 2i\omega\frac{\partial}{\partial t} - \omega^2\Big)\Big\}E(z,t)e^{-i(\omega t - kz)}$$
$$= \hat{p}\mu_o\Big(\frac{\partial^2}{\partial t^2} - 2i\omega\frac{\partial}{\partial t} - \omega^2\Big)P^{NL}(z,t)e^{-i(\omega t - k_p z)}. \tag{2.69}$$

Using the definition $k^2 = \mu_o\epsilon\omega^2$ and assuming the envelopes are slowly varying, the higher order derivatives are much smaller than the lower order derivatives. We can assume:

$$k\frac{\partial E(z,t)}{\partial z} \gg \frac{\partial^2 E(z,t)}{\partial z^2} \tag{2.70}$$

$$\omega\frac{\partial E(z,t)}{\partial t} \gg \frac{\partial^2 E(z,t)}{\partial t^2} \tag{2.71}$$

$$\omega^2 P^{NL}(z,t) \gg \omega\frac{\partial P^{NL}}{\partial t}(z,t) \gg \frac{\partial^2 P^{NL}(z,t)}{\partial t^2}. \tag{2.72}$$

Equation (2.69) then becomes

$$\Big\{2ik\frac{\partial}{\partial z} + 2i\omega\mu_o\epsilon\frac{\partial}{\partial t}\Big\}E(z,t)e^{-i(\omega t - kz)} = -(\hat{e}\cdot\hat{p})\mu_o\omega^2 P^{NL}(z,t)e^{-i(\omega t - k_p z)}. \tag{2.73}$$

We divide through by $-2ik$ and obtain

$$(\frac{\partial}{\partial z} + \mu_o\epsilon\frac{\omega}{k}\frac{\partial}{\partial t})E(z,t)e^{-i(\omega t-kz)} = (\hat{e}\cdot\hat{p})\frac{i\mu_o\omega^2}{2k}P^{NL}(z,t)e^{-i(\omega t-k_p z)}. \tag{2.74}$$

We collect the phases and simplify to

$$(\frac{\partial}{\partial z} + \mu_o\epsilon\frac{\omega}{k}\frac{\partial}{\partial t})E(z,t) = (\hat{e}\cdot\hat{p})\frac{i\mu_o\omega^2}{2k}P^{NL}(z,t)e^{-i(k-k_p)z}. \tag{2.75}$$

Recall $\frac{\omega}{k} = \frac{c}{n}$ and $\mu_o\epsilon = \left(\frac{n}{c}\right)^2 = \left(\frac{k}{\omega}\right)^2$, and substitute these definitions into Equation (2.75) to obtain

$$(\frac{\partial E}{\partial z} + \frac{n}{c}\frac{\partial E}{\partial t}) = (\hat{e}\cdot\hat{p})\frac{i\mu_o c}{2n}\omega P^{NL}e^{-i(k-k_p)z}. \tag{2.76}$$

If we consider the steady-state solutions ($\frac{\partial}{\partial t} = 0$) and assume the field and nonlinear polarization are copolarized, we obtain

$$\frac{\partial E}{\partial z} = \frac{i\omega\mu_o c}{2n}P^{NL}e^{-i(k-k_p)z}. \tag{2.77}$$

This equation can actually be expanded into a set of coupled-wave equations which describe the propagation of fields for particular processes. For example, for the third order process of cross-phase modulation, we can write the polarization as

$$\mathbf{P}(\omega_2 = \omega_1 + \omega_2 - \omega_1) = \epsilon_o\chi^{(3)}(\omega_2 : \omega_1, \omega_2, -\omega_1)\mathbf{E}(\omega_1)\mathbf{E}(\omega_2)\mathbf{E}^*(\omega_1) \tag{2.78}$$

We also need to write out equations for $\mathbf{P}(\omega_1)$:

$$\mathbf{P}(\omega_1 = \omega_2 - \omega_2 + \omega_1) = \epsilon_o\chi^{(3)}(\omega_1 : \omega_2, -\omega_2, \omega_1)\mathbf{E}(\omega_2)\mathbf{E}^*(\omega_2)\mathbf{E}(\omega_1) \tag{2.79}$$

Substituting Equation (2.78) into Equation (2.77), we obtain the coupled-wave equation that describes cross-phase modulation.

$$\frac{\partial E(\omega_1)}{\partial z} = \frac{i\omega_1 d}{n_1 c} E(\omega_1) E^*(\omega_2) E(\omega_2) \tag{2.80}$$

$$\frac{\partial E(\omega_2)}{\partial z} = \frac{i\omega_2 d}{n_2 c} E(\omega_2) E^*(\omega_1) E(\omega_1) \tag{2.81}$$

where $d = \frac{1}{2}\chi$ and is a scalar coefficient that accounts for the tensor qualities of χ and $\Delta k = k - k_p = 0$. The process is automatically phase-matched. It may be thought of as $|E(\omega_1)|^2$ changing the index of refraction seen by $E(\omega_2)$.

2.3 The Nonlinear Schrödinger Equation

The coupled-wave equations do not account for propagation of a pulse with non-negligible bandwidth. In this section, we consider optical pulse propagation in fiber again, but now we take into account the propagation of a pulse with non-negligible bandwidth. In this example, the dominant nonlinear effect experienced by the pulse will be SPM becasue that process is automatically phase-matched. Recall from Section 2.1.1 the nonlinear polarization for self-phase modulation:

$$P_x^{(3)}(\omega) = \frac{3\epsilon_o}{4}\{\chi_{xxxx}^{(3)}(\omega : \omega, \omega, -\omega)|E_1(\omega)|^2 E_1(\omega). \tag{2.82}$$

Substituting this relation into Equation (2.77) and noting that this process is phase-matched, we obtain

$$\frac{\partial}{\partial z} E(\omega) = \frac{3}{8}\frac{i\omega}{n_o c}\chi^{(3)}(\omega)|E(\omega)|^2 E(\omega). \tag{2.83}$$

Now, we consider a short pulse, which has a finite bandwidth. Each frequency component propagates as $e^{ik(\omega)z}$, where $k(\omega)$ is frequency dependent (since ϵ is frequency dependent). In fiber, as mentioned earlier, we approximate the wave number $k(\omega)$ by the propagation constant $\beta(\omega)$. We expand $\beta(\omega)$ in a Taylor series around ω:

$$\beta(\omega) = \beta(\omega_o) + \left.\frac{\partial\beta(\omega)}{\partial\omega}\right|_{\omega_o}(\omega - \omega_o) + \frac{1}{2}\left.\frac{\partial^2\beta(\omega)}{\partial\omega^2}\right|_{\omega_o}(\omega - \omega_o)^2 + ... \tag{2.84}$$

The form of our electric field (Equation (2.63)) in fiber becomes

$$E(z, \omega, t) = E(z, t)e^{-i(\omega t - \beta z)}, \tag{2.85}$$

where we have dropped our vector notation for simplicity. The corresponding Fourier Transform is

$$E(z, \omega, t) = E(z, \omega - \omega_o)e^{i\beta(\omega_o)z}. \tag{2.86}$$

To discover how this pulse propagates in fiber, we consider an incrementally small length Δz. The change in the electric field over this small length is then

$$\Delta E = [i\beta(\omega) - i\beta(\omega_o)]E\Delta z, \tag{2.87}$$

which becomes

$$\frac{\partial E}{\partial z} = i[\beta(\omega) - \beta(\omega_o)]E. \tag{2.88}$$

Substituting in Equation (2.84), Equation (2.88) becomes

$$\frac{\partial E}{\partial z} = i\left[\left.\frac{\partial \beta}{\partial \omega}\right|_{\omega_o}(\omega-\omega_o) + \frac{1}{2}\left.\frac{\partial^2 \beta}{\partial \omega^2}\right|_{\omega_o}(\omega-\omega_o)^2 + ...\right]E. \tag{2.89}$$

Now we transform this equation back to the time domain. Multiplication by $-i(\omega - \omega_o)$ in frequency transforms to $\frac{\partial}{\partial t}$ in time.

$$\frac{\partial E}{\partial z} = -\left.\frac{\partial \beta}{\partial \omega}\right|_{\omega_o}\frac{\partial}{\partial t}E - i\frac{1}{2}\left.\frac{\partial^2 \beta}{\partial \omega^2}\right|_{\omega_o}\frac{\partial^2}{\partial t^2}E + ... \tag{2.90}$$

We will ignore third order terms and higher from now on, since they are simple enough to add later. We consider some definitions:

$$\left.\frac{\partial \beta}{\partial \omega}\right|_{\omega_o} = \frac{1}{v_g} \tag{2.91}$$

$$\left.\frac{\partial^2 \beta}{\partial \omega^2}\right|_{\omega_o} = \beta_2, \tag{2.92}$$

where v_g is the group-velocity and β_2 describes the group-velocity dispersion. Combining our results from Equations (2.83) and (2.90)-(2.92), we obtain the nonlinear Schrödinger's equation:

$$\frac{\partial E}{\partial z} + \frac{1}{v_g}\frac{\partial E}{\partial t} = -i\frac{1}{2}\beta_2\frac{\partial^2 E}{\partial t^2} + i\gamma|E|^2E, \tag{2.93}$$

where γ is defined as $\frac{3\omega}{8cn_o}\chi^{(3)}$. The second term on the left side of Equation (2.93) is the group velocity term, which tells us that the pulse is propagating at a certain velocity (v_g). The first term on the right hand side describes the group velocity dispersion. As a pulse propagates in fiber, group velocity dispersion causes the different frequency components of the pulse to travel at different speeds. As a result of this effect, the pulse broadens out in time. The second term on the right hand side of

Equation (2.93) describes the nonlinear effects in the fiber due to self-phase modulation. As described in Section 2.1.1, this nonlinearity induces an intensity-dependent phase in the pulse. As a result, pulses end up chirped and the phase of the pulse varies across the pulse itself. The nonlinear Schrödinger equation is often taken to a moving reference frame and normalized; for further details, please refer to chapter 3 in Agarwal's book.[15]

Thus far, we have not considered the effect of loss on the propagation of pulses through fiber. We model loss as an exponential term:

$$P_o = P_i e^{-\alpha z}, \tag{2.94}$$

where P_i is the power going into and P_o is the power coming out of a length z of fiber.[15] When α is positive, it describes loss. When it is negative, however, it describes a gain in the medium. Power is related to the square of the electric field, so the loss in terms of the electric field is

$$E_o = E_{in} e^{-\frac{\alpha}{2} z}. \tag{2.95}$$

If we take the derivative of this, we obtain

$$\begin{aligned} \frac{\partial E_o}{\partial z} &= -E_{in} \frac{\alpha}{2} e^{-\frac{\alpha}{2} z} \\ &= -\frac{\alpha}{2} E_o. \end{aligned} \tag{2.96}$$

Thus, we can include this in the nonlinear Schrödinger equation (Equation (2.93)) to

obtain

$$\frac{\partial E}{\partial z} + \frac{1}{v_g}\frac{\partial E}{\partial t} = -i\frac{1}{2}\beta_2\frac{\partial^2 E}{\partial t^2} - \frac{\alpha}{2}E + i\gamma|E|^2 E. \tag{2.97}$$

Chapter 3

FROG Pulse Characterization Theory

Examination of the nonlinear Schrödinger equation (2.97) indicates that pulse propagation through fiber is a complicated process. Mathematically, analytic solutions to Equation (2.97) are dificult to find (with the exception of the well-known soliton solution) and numerical techniques are generally required to estimate the effects of the interplay between group velocity dispersion, fiber loss, and nonlinearity. In the laboratory, characterization of optical pulses is absolutely required as channel rates increase and pulse widths used in communication systems decrease. Our interest is in the characterization of pulses in the picosecond regime which have proven to be challenging due to their small bandwidth and small time duration.

Pulse characterization requires exact measurement of the pulse envelope and spectral phase content. From these measurements, useful parameters can be calculated, such as pulse width, pulse intensity, and chirp. Traditional measurement techniques

rely on the use of optical autocorrelation to determine the temporal pulse width and spectral analysis to determine the bandwidth of the pulse. These techniques, however, are fairly limited in their accuracy. In fact, this characterization technique is only accurate when the measured pulse is transform-limited (has no chirp). Equation (2.97) indicates that unchirped pulse propagation is difficult to achieve in optical fiber for short pulses due to the presence of intensity-dependent SPM nonlinearity. In addition, the symmetric response of the autocorrelation also means that asymmetric distortions in the pulse will not be identified correctly. As shown previously in Chapter 2, pulse distortions can result from linear effects such as group velocity dispersion and chirp induced by the nonlinearities of the medium, which generally results in an increased number of errors in the communications network. Because this distortion ultimately limits system performance, the ability to accurately and completely characterize a short optical pulse is required if we hope to extend transmission distances in optical networks. A new method called Frequency-Resolved Optical Gating (FROG),[10,13] has been developed to provide accurate measurements of short pulses. Specifically, it has been developed to provide simple characterization of ultrashort pulses with $\tau < 100$fs.

3.1 Autocorrelation

The optical autocorrelation is given by:

$$A(\tau) = \int_{-\infty}^{\infty} I(t)I(t-\tau)dt \tag{3.1}$$

where $I(t)$ is the intensity of the pulse under test. Physically, we split the pulse into two identical copies of itself, and then spatially overlap the two copies together inside a noncentrosymmetric $\chi^{(2)}$ crystal optimized for second harmonic generation (SHG) (Figure 3.1). The crystal should be oriented to maximize the phase-matching

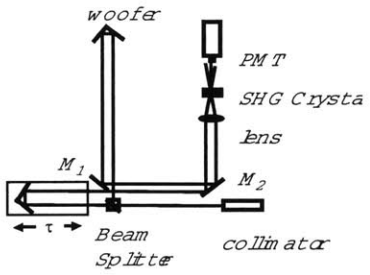

Figure 3.1: Experimental setup for the measurement of optical pulses using optical autocorrelation. (fig/autocorrsetup.eps)

to obtain a strong sum harmonic signal. This requirement is met by orienting the crystal such that the dispersion of the refractive index is compensated by the crystal birefringence effect.

The crystal will produce a pulse at twice the frequency of the original pulse with an intensity proportional to the product of the input intensities. This second order process is the sum harmonic generation, and is given by

$$\mathbf{P}^{(2)}(\omega_1 + \omega_2) = 2\chi^{(2)}(\omega_1 + \omega_2)\mathbf{E}_1\mathbf{E}_2. \tag{3.2}$$

In the case of an autocorrelation, $\omega_1 = \omega_2$. Integrating the output of the crystal will then give us the autocorrelation of the pulse. We perform the integration by passing the sum harmonic field into a photodetector, which integrates the results and passes it

to an oscilloscope to be displayed. A rough estimate of the pulse length can be made by observing the full width at half max (FWHM) of the autocorrelation output. This estimate can be further refined by measuring the spectrum of the pulse and calculating the time-bandwidth product, as explained in Section 3.2. The autocorrelation is also useful in detecting the presence of distortions that would affect the intensity envelope of the pulse.

The resolution of the autocorrelator is related to both the step size of the stage as well as the bandwidth of the nonlinear crystal. The stage controls the overlap of the two pulses and the step size determines how closely spaced our measurements are. In the laboratory, our stages have step sizes of 10 μ m, which corresponds to a step size of approximately 0.8 fs. This is plenty of resolution for pulses on the order of a few picoseconds. The bandwidth of the nonlinear crystal also needs to be large enough to accommodate the pulse bandwidth. If not, the pulses will be distorted as they are passed through the crystal, and an accurate autocorrelation will not be possible.

The shortcomings of the autocorrelation are readily apparent. It is clear that any autocorrelation will result in a symmetric output regardless of the input pulse asymmetries. Furthermore, the autocorrelation will always only give information about the pulse intensity, omitting any information about pulse phase or chirp. However, more information about a pulse can be obtained when the autocorrelation is used in conjunction with spectral measurements of the pulse.

3.2 Spectral Measurements

The spectrum of a pulse is easily obtained using a spectrometer. Spectrometers, monochromators, and spectrum analyzers are all based on the concept of using a grating to spatially separate the different frequency components of a pulse. A grating is a reflective piece of material which is usually scored with thin lines. When light hits these lines, it reflects off in a range of angles. At certain angles, light of a specific wavelength will interfere constructively. Other wavelengths will constructively interfere at other angles. This has the overall effect of separating the wavelengths in the incoming light.[18] The general equation for a diffraction grating is

$$m\lambda = d(\sin\alpha - \sin\beta), \tag{3.3}$$

where m is the diffraction order, λ is the wavelength of interest, d is the grating period, α is the angle of the incident light with respect to the grating normal, and β is the angle the diffracted light makes with the grating normal. Figure 3.2 is a diagram which illustrates grating operation. The resolution of a spectrometer is determined by the amount of dispersion given by the diffraction grating. The angular dispersion measures how widely separated two different wavelengths are, and is given by differentiating the grating equation and assuming the incident angle is fixed. We obtain

$$\frac{d\beta}{d\lambda} = -\frac{m}{d\cos\beta}. \tag{3.4}$$

We are generally more interested in the measure of linear dispersion, which tells us how widely spaced the different wavelengths are at the focal plane of detection. The more

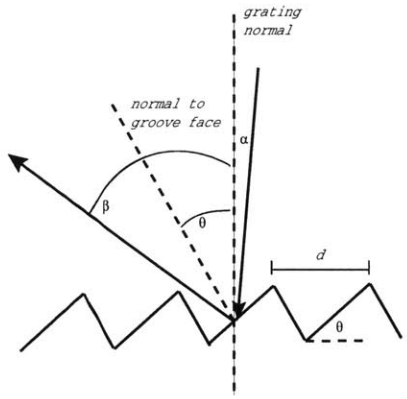

Figure 3.2: Cross-section diagram of grating and angles associated with it. α is the angle of incidence of the light, θ is the blaze angle, β is the angle of diffraction, and d is the grating period.[19] (fig/gratingeq.eps)

widely spaced adjacent wavelengths are, the more easily we can distiguish between them. This gives us an idea as to the resolution of the spectrometer. To calculate the linear dispersion, we multiply the angular dispersion with the focal length of the spectrometer.

$$\frac{dx}{d\lambda} = \frac{d\beta}{d\lambda} f. \tag{3.5}$$

A spectrometer can be used in order to increase the accuracy of pulse characterization measurements over those made with an autocorrelator alone. A fairly accurate estimate of the pulse length can be made by first assuming the pulse is transform limited. This statement means that the Fourier transform of the real portion of the E field is the same as the Fourier transform of the complex E field of the pulse. Transform-limited also implies that no chirp exists for the pulse. In order to determine when a pulse is transform-limited, we consider the time-bandwidth product $\Delta\omega\Delta t$. However,

this relation is different for different pulse shapes (gaussian, sech, etc.). The traditional method of determining if a pulse is transform limited is to make an estimate as to the pulse shape (gassian, sech, etc), and then to find if the time-bandwidth product is close to what it would be if it were transform-limited. If the time-bandwidth product indicates that the pulse is near transform-limited, we can assume it is transform limited. We can calculate the relation between the FWHM of an autocorrelation of a pulse and the pulse length provided the pulse is transform-limited. This also requires the assumption of a pulse shape. If the time-bandwidth product indicates that the pulse is not transform-limited, we cannot calculate the relation between the FWHM of its autocorrelation and the pulse length without knowing the extent of the chirp. As a result, non-transform-limited pulse lengths are impossible to characterize using only an autocorrelator and a spectrometer. Table 3.1 shows the time-bandwidth product and the relation between the pulse length and autocorrelation FWHM for a few common pulse shapes.

Even if a spectrometer is added to the measurment, pulse characterization using autocorrelation obviously requires many assumptions, which may or may not be correct. Furthermore, if the pulse is not transform-limited and has been severely distorted, no reliable way of arriving at a measurement of pulse length using the autocorrelation has been found. In order to solve all these problems, FROG was developed to characterize ultrashort pulses in the femtosecond regime.

3.3 Frequency-Resolved Optical Gating

The idea of a spectrogram has been present in acoustics for a while before being applied to the field of optical communications.[20] However, the significance was not yet

Field Envelope	Intensity Profile	τ_{FWHM}	τ_{ac}	Spectral profile	ω_{FWHM}	$\tau_{\text{FWHM}}\omega_{\text{FWHM}}$
Gaussian	$e^{-2(\frac{t}{\tau_o})^2}$	$1.77\tau_o$	$1.414\tau_{\text{FWHM}}$	$e^{-\frac{(\Omega\tau_o)^2}{2}}$	$\frac{2.355}{\tau_o}$	0.441
Sech	$\text{sech}^2(\frac{t}{\tau_o})$	$1.763\tau_o$	$1.543\tau_{\text{FWHM}}$	$\text{sech}^2(\frac{\pi\Omega\tau_o}{2})$	$\frac{1.122}{\tau_o}$	0.315

Table 3.1: Time Bandwidth product and autocorrelation FWHM for gaussian and sech pulses.

clear until it was shown that the spectrogram of a pulse could be used to reconstruct its intensity and phase.[21] The spectrogram characterization technique was further refined into the current FROG method as developed by Daniel Kane, Kenneth DeLong, and Rick Trebino.[8–10] Since then, many different variations in FROG measurement techniques have been developed.[11,12,22,23]

The theory behind FROG is fairly simple. In order to completely characterize the pulse under test, both time and spectral information must be measured simultaneously. A spectrogram of the pulse plots the pulse spectral content versus the pulse temporal characteristics, as shown in Figure 3.3. To obtain a spectrogram, we first gate the original pulse $E(t)$ with some gating function $g(t)$. This produces one slice in time of the original pulse. We then take the spectrum of this slice in time. By varying the delay of $g(t)$ with respect to $E(t)$, we can obtain the spectrum of each slice of $E(t)$. Plotting these slices in order, we obtain a plot of both the spectral content and temporal content of the pulse. It is clear that the gating function will determine the temporal and spatial resolution of the spectrogram, and thus the choice of $g(t)$ is very important. Different FROG techniques choose different gating functions. The spectrogram is given by

$$S(\omega,\tau) = \left| \int_{\infty}^{\infty} E(t)g(t-\tau)e^{-i\omega t}dt \right|^2 . \tag{3.6}$$

With the spectrogram, we can completely determine the original pulse, save for an absolute phase factor. This phase factor is not of much interest to us, though it is useful in performing absolute frequency locking of ultrashort pulse lasers.[24] In order to determine the phase of the pulse from a FROG spectrogram, an iterative algorithm is used. This process will be described in Section 3.3.3.

3.3.1 Methods for Obtaining a Trace

Many different possible methods exist to acquire a spectrogram in the laboratory. The easiest to implement is perhaps the second harmonic generation (SHG) FROG, in which the spectrogram is obtained simply by observing the spectrum of the autocorrelation of the pulse. In this case, the gating function is the pulse itself

$$I_{FROG}^{SHG}(\omega,\tau) = \left| \int_{\infty}^{\infty} E(t)E(t-\tau)e^{-i\omega t}dt \right|^2. \tag{3.7}$$

This results in a spectrogram that is very sensitive, but somewhat unintuitive because the direction of time is unclear in the spectrograms from SHG FROG. This statement means that it is impossible to tell (without other measurements) whether a pulse is positively or negatively chirped due to the fact that the autocorrelation of the pulse is used. Other FROG methods include PG (polarization gate) FROG, in which the gate and pulse under test are polarized at 45^o before being sent through a piece of fused silica. SD (self-diffraction) FROG has a configuration in which the gate and original pulses are sent through fused silica with the same polarization. TG (transient grating) FROG splits the original pulse in three ways, using two of the signals to induce a material grating through which the third pulse is diffracted. Finally, THG (third harmonic generation) FROG uses a glass plate to induce a surface third harmonic generation in response to the pulses. See Table 3.2[8] for a comparison of the different types of FROG methods.

The challenge for any FROG method we choose to implement will be to adequately resolve the pulses we are currently using in the laboratory. The system must be fairly sensitive in order to observe low energy pulses with relatively small bandwidth. (For example, if we consider a 2 ps pulse train at 10 mW with a repetition rate of 10 Gb/s,

the average energy is 1pJ and the pulse bandwidth is approximately 1.5nm.) These requirements suggest that SHG FROG is worth investigating for picosecond pulse characterization, since it is the most sensitive of the FROG pulse characterization family.

3.3.2 Simulations of FROG Traces

In order to examine the output spectrogram from an SHG FROG pulse characterization setup, we can simulate several different cases based on unchirped and chirped pulses with gaussian and sech envelope shapes. The results of these simulations are shown in the following figures. As mentioned before, the SHG FROG pulse characterization results in traces which are symmetric in time. Even so, we can easily distinguish between a chirped pulse and a nonchirped pulse, as is clear from comparing Figures 3.3 (an unchirped gaussian) and 3.4 (a gaussian with cubic phase). Both figures show pulses with a FWHM of 2ps. We also show the FROG traces for an unchirped hyperbolic secant pulse (Figure 3.5) and for a hyperbolic secant pulse with cubic phase (Figure 3.6). Again, both traces are of pulses with a FWHM of 2ps.

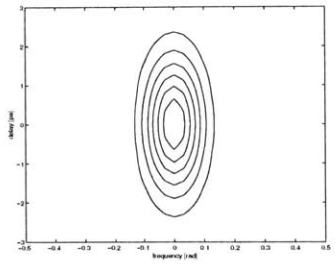

Figure 3.3: Simulation of a SHG FROG trace taken of a gaussian pulse with no chirp and a FWHM of 2ps. (fig/gaussnochirpfrog.eps)

	PG FROG	SD FROG	TG FROG	THG FROG	SHG FROG
Nonlinearity Sensitivity	$\chi^{(3)}$	$\chi^{(3)}$	$\chi^{(3)}$	$\chi^{(3)}$	$\chi^{(3)}$
Singleshot sensitivity	$\sim 1\mu J$	$\sim 10\mu J$	$\sim 0.1\mu J$	$\sim 0.03\mu J$	$\sim 0.01\mu J$
Multishot sensitivity	$\sim 100nJ$	$\sim 1000nJ$	$\sim 10nJ$	$\sim 3nJ$	$\sim 0.001nJ$
Advantages	Intuitive traces, Automatic phase matching	Intuitive traces	Intuitive traces, Sensitive, Background free	Very large bandwidth, Sensitive	Simple to build, Very sensitive
Disadvantages	Requires polorizers	Requires thin medium, Not phase matched	Three beams	Unintuitive traces	Unintuitive traces
Ambiguities	-	-	-	Relative phases of multiple pulses	Direction of time Relative phases of multiple pulses
Trace	$\left\|\int_\infty^\infty E(t)\|E(t-\tau)\|^2 e^{-i\omega t}dt\right\|^2$	$\left\|\int_\infty^\infty E^2(t)E*(t-\tau)e^{-i\omega t}dt\right\|^2$	Either PG or SD trace	$\left\|\int_\infty^\infty E^2(t)E(t-\tau)e^{-i\omega t}dt\right\|^2$	$\left\|\int_\infty^\infty E(t)E(t-\tau)e^{-i\omega t}dt\right\|^2$

Table 3.2: Summary of Different FROG Geometries [8]

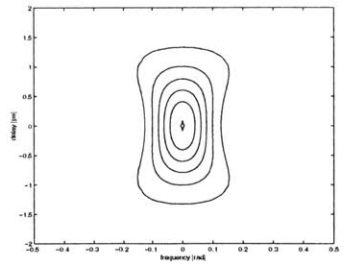

Figure 3.4: Simulation of a SHG FROG trace taken of a gaussian pulse with a cubic phase and a FWHM of 2ps. (fig/gausstripchirpfrog.eps)

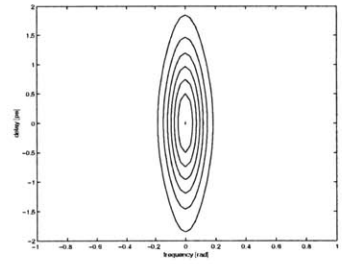

Figure 3.5: Simulation of a SHG FROG trace taken of a sech pulse with a no chirp and a FWHM of 2ps. (fig/sechnochirpfrog.eps)

3.3.3 Extracting Phase and Amplitude

As described previously, the measurement of pulse phase is impossible with traditional measurement options such as the autocorrelation. With the FROG spectrogram, however, an iterative pulse retrieval algorithm has been developed which is fairly robust and general[10,13,25,26] The FROG spectrogram problem is in fact identical to the two-dimensional phase retrieval problem, which has been solved previously in image processing applications .[27–29] In only one dimension, it is impossible to retrieve the phase of a signal from its magnitude. However, in two dimensions, enough information

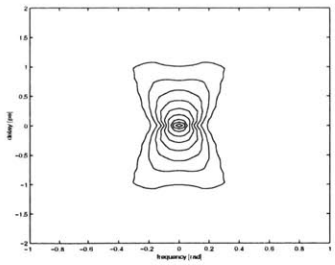

Figure 3.6: Simulation of a SHG FROG trace taken of a sech pulse with a cubic phase and a FWHM of 2ps. (fig/sechtripchirpfrog.eps)

is provided that this is possible. The FROG algorithm is based on the method of generalized projections, in which an initial guess is taken, and then constraints are applied through an iterative process until the solution converges. In our case, we are looking for the $E(t)$ that would produce the FROG trace we have experimentally measured, where

$$E_{sig}(t,\tau) = E(t)g(t-\tau). \tag{3.8}$$

And in the case of SHG FROG,

$$E_{sig}(t,\tau) = E(t)E(t-\tau). \tag{3.9}$$

The trial solution E_{sig} must obey two constraints. First, E_{sig} needs to match the experimental data we have from the FROG trace. Second, E_{sig} must be a physically realizable product of some $E(t)$ and $E(t-\tau)$. One possible implementation of this algorithm is as follows:

1. We choose a trial solution $E(t)$.

2. We form the trial solution $E_{sig}(t,\tau)$.

3. We find the Fourier transform, producing $E_{sig}(\omega,\tau)$.

4. We then apply the first constraint by replacing the magnitude of the trial solution with the magnitude of the experimental data:

$$E'_{sig}(\omega,\tau) = \frac{E_{sig}(\omega,\tau)}{|E_{sig}(\omega,\tau)|}[I_{FROG}(\omega,\tau)]^{\frac{1}{2}}. \tag{3.10}$$

5. Next, we take the inverse Fourier transform of this, ending up with $E'_{sig}(t,\tau)$.

6. We then take the projection of that onto $E'(t)E'(t-\tau)$ by minimizing:

$$Z = \varsigma^{N}_{t,\tau=1}|E'_{sig}(t,\tau) - E'(t)E'(t-\tau)|^2. \tag{3.11}$$

   This gives us a new trial solution $E(t)$.

7. We repeat this process until our solution converges to a satisfactory degree, where we define the convergence criteria as:

$$G = \left\{\frac{1}{N^2}\varsigma^{N}_{\omega,\tau=1}\left[I_{FROG}(\omega,\tau) - |E_{sig}(\omega,\tau)|^2\right]^2\right\}^{1/2}. \tag{3.12}$$

In this case, both I_{FROG} and E_{sig} are normalized to unity before G is computed. In previous experiments on this subject, it was found that a value of G less than 0.0001 results in a retrieved field which is visually indistinguishable from the originally measured field.[25]

Chapter 4

Interferometric Pulse Characterization Theory

Characterization of picosecond pulses is challenging due to small bandwidth and low power. The challenge for the SHG FROG is to achieve enough resolution in the frequency domain with such low power. Another method, using spectral interferometry, may to overcome these difficulties.

This interferometric method, developed by Jean Debeau et. al.,[7] extracts the optical pulse phase using only an RF phase delay and an electro-optic modulator. The sinusoidal drive signal to the modulator is at exactly half the frequency of the pulse train. A variable time delay is included in the modulation signal path. A diagram of the experimental setup of this method is shown in Figure 4.1. The result is that each of the frequency components spaced by the repetition rate in the original pulse train spectrum will mix up and down by half of the pulse train repetition rate to new frequency components. By adjusting the variable time delay and measuring

the new frequency components on an optical spectrum analyzer, we can extract the spectral phase of the original frequency components. From the spectral phase, it is a simple Fourier transform to obtain the temporal phase. As mentioned in Chapter 2,

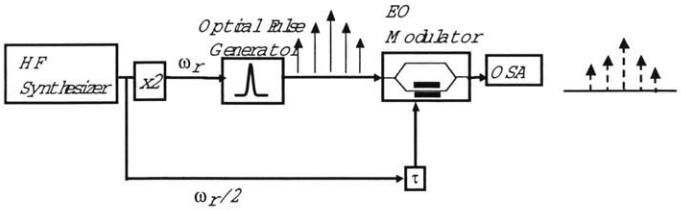

Figure 4.1: Experimental setup for the measurement of optical pulses in the picosecond regime using the spectral interferometric method as introduced by Debeau.[7] (fig/specintsetup.eps)

a pulse can be represented as

$$\mathbf{E}(z,\omega,t) = \hat{\mathbf{e}}E(z,t)e^{-i(\omega t - kz)} \tag{4.1}$$

where $E(z,t)$ is a slowly varying envelope. For analysis of this method, we assume gaussian pulses in a pulse train with a repetition rate of $T_r = \frac{1}{f_r} = \frac{2\pi}{\omega_r}$. We drop the spatial dependence for simplicity and represent the pulse train as

$$E(t) = A_{in}e^{\frac{-t^2}{2\tau^2}} * \sum_k \delta(t - kT_r). \tag{4.2}$$

To find the spectrum of this pulse train, we note that a convolution in time is equivelent to a multiplication in frequency. Thus, we can take the Fourier transform of an individual pulse and multiply that with the Fourier transform of the impulse train.

The Fourier transform of the individual gaussian pulse is also a gaussian

$$\mathrm{FT}\left\{ A_{in} e^{\frac{-t^2}{2\tau^2}} \right\} = A_{in} e^{\frac{-\omega^2 \tau^2}{2}}, \tag{4.3}$$

and the Fourier transform of an impuse train is another impulse train

$$\mathrm{FT}\left\{ \sum_{n=-\infty}^{\infty} \delta(t - nT_r) \right\} = \frac{2\pi}{T_r} \sum_{k=-\infty}^{\infty} \delta(\omega - \frac{2\pi k}{T_r}) \tag{4.4}$$

If we multiply the two Fourier transforms, we obtain the spectrum of the gaussian pulse train, which is a series of spectral lines overlaid by a gaussian envelope.

$$E_{in}(\omega) = A_{in} \frac{2\pi}{T_r} e^{\frac{-\omega^2 \tau^2}{2}} \sum_{k=-\infty}^{\infty} \delta(\omega - \frac{2\pi k}{T_r}) \tag{4.5}$$

A simulation of a pulse train of 15ps gaussian pulses at a repetition rate of 10GHz and its corresponding spectrum is shown in Figure 4.2. We can simplify Equation (4.5) by writing the amplitude and phase associated with each spectral line by E_k. We also add a carrier frequency ω_o, since our pulse train is centered around a particular frequency.

$$E_{in}(\omega) = \sum_k E_k \delta[\omega - (\omega_o + \frac{2\pi k}{T_r})]. \tag{4.6}$$

More specifically, we write

$$E_k = A_k e^{-i\Phi_k}, \tag{4.7}$$

where A_k is the amplitude and Φ_k is the phase of the kth spectral line.

Let us now consider the setup of this pulse characterization method as described

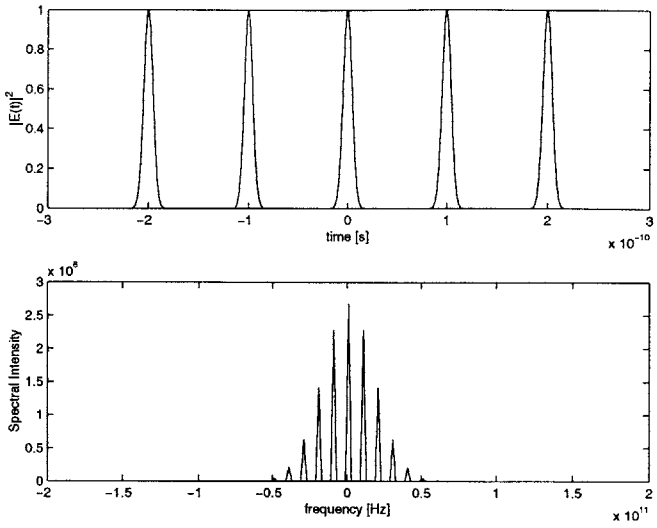

Figure 4.2: Example of a pulse train (top) and its spectrum (bottom). The pulse train has a repetition rate of 10GHz, and the pulses have a FWHM of 15ps. (fig/pulsetrainandspectrum.eps)

in Figure 4.1. To analyze the result of this setup, we must take the pulse train created by the optical pulse generator and pass it through the electro-optic modulator. We then look at the spectral intensity at the output of the electro-optic modulator. Thus, we are interested in the transfer function of an electro-optic modulator sinusoidally driven at half the frequency of the input optical pulse train. A diagram of the electro-optic modulator is shown in Figure 4.3. The modulator is simply an interferometor with a phase delay on one arm. When the light enters the modulator, its power is split into two halves. One half incurs only the phase shift due to propagation down the length of that arm of the modulator. The other half experiences an additional electro-optically induced phase shift which results in a differential phase delay of $e^{-i\phi(t)}$, where $\phi(t)$ is the modulation drive signal. The two halves are recombined at the output of the modulator. From this, we see that the transfer function for the

optical field in the electro-optic modulator takes the form

$$\frac{E_{out}}{E_{in}} = T(t) = 1 + e^{-i\phi(t)}. \tag{4.8}$$

We will now calculate the output of the EO modulator in the spectral domain given

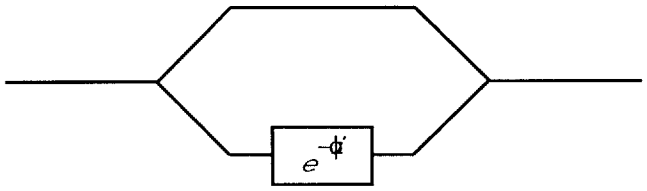

Figure 4.3: Diagram of an electro-optic modulator. Incoming light is split into two arms; one arm allows the light to pass through without change while the other arm induces a phase shift. The light is recombined at the output.
(fig/eomod.eps)

our setup. In our case, the modulation drive signal is

$$\phi(t) = \frac{\pi}{V_{pi}}\left\{V_m \cos\left[\frac{\omega_r}{2}(t-\tau)\right] + V_b\right\}, \tag{4.9}$$

where V_π is a function of the physics of the electro-optic modulator and indicates the constant voltage at which the second arm incurs a π phase shift. In other words, V_π indicates the voltage at which the output of the modulator is at a null. V_m is simply the amplitude of the modulation drive signal. Finally, V_b is a constant DC bias voltage. Substituting this drive signal in Equation (4.8), we obtain

$$T(t) = 1 + e^{-i\frac{\pi}{V_\pi}\left\{V_m \cos\left[\frac{\omega_r}{2}(t-\tau)\right] + V_b\right\}}, \tag{4.10}$$

Let us assume that we bias the modulator at the null, which implies $V_b = V_\pi$. Equa-

tion (4.10) then becomes

$$T(t) = 1 + e^{-i\left(\frac{\pi V_m}{V_{pi}} \cos\left[\frac{\omega_r}{2}(t-\tau)\right] + \pi\right)} \tag{4.11}$$
$$= 1 - e^{-i\left(\frac{\pi V_m}{V_{pi}} \cos\left[\frac{\omega_r}{2}(t-\tau)\right]\right)}.$$

For convenience, let us define

$$\phi'(t) = \frac{\pi V_m}{V_\pi} \cos\left[\frac{\omega_r}{2}(t-\tau)\right]. \tag{4.12}$$

We then factor out $e^{-i\frac{\phi'(t)}{2}}$ and Equation (4.11) then becomes

$$T(t) = e^{-i\frac{\phi'(t)}{2}}\left(e^{i\frac{\phi'(t)}{2}} - e^{-i\frac{\phi'(t)}{2}}\right). \tag{4.13}$$

Simplifying, we get

$$T(t) = e^{-i\frac{\phi'(t)}{2}} 2i \sin(\frac{\phi'(t)}{2}) \tag{4.14}$$
$$= 2e^{-i\frac{1}{2}(\phi'(t)+\pi)} \sin(\frac{\phi'(t)}{2}).$$

If we assume the amplitude of $\phi'(t)$ is small (V_m is less than 30% of V_π), we can approximate $\sin(\frac{1}{2}\phi'(t))$ as simply $\frac{1}{2}\phi'(t)$. Equation (4.14) then becomes

$$T(t) = e^{-i\frac{1}{2}(\phi'(t)+\pi)}\phi'(t) \tag{4.15}$$
$$= e^{-i\frac{1}{2}(\phi'(t)+\pi)}\frac{\pi V_m}{V_{pi}} \cos\left[\frac{\omega_r}{2}(t-\tau)\right]$$
$$= m\frac{\pi V_m}{V_\pi} cos\left[\frac{\omega_r}{2}(t-\tau)\right],$$

where m is a time-dependent phase. However, we have assumed that the amplitude of the time-dependence of this phase $\phi'(t)$ is small compared to pi. If this is true, then we can ignore the time-dependence of this phase. The intensity transfer function is then

$$|T(t)|^2 = \left(\frac{\pi V_m}{V_{pi}}\right) \cos^2 \left[\frac{\omega_r}{2}(t-\tau)\right]. \tag{4.16}$$

Note that in observing the intensity spectrum, the phase term m disappears. The intensity transfer function is simply a raised cosine and is plotted in Figure 4.4, where we have assumed $\tau = 0$, $\frac{\pi V_m}{V_{pi}} = 1$, and $\omega_r = 2pi * 10\text{GHz}$.

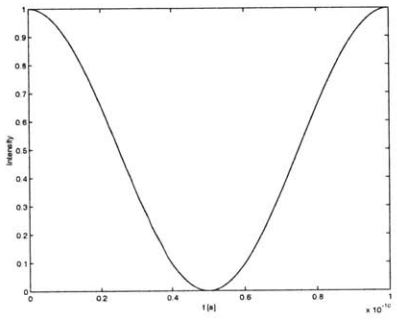

Figure 4.4: Plot of intensity transfer function of an electro-optic modulator sinusoidally driven at $0.5\omega_r$, where ω_r corresponds to a linear frequency of 10GHz, τ is zero, and the amplitude $\frac{\pi V_m}{V_{pi}}$ is one. (fig/raisedcosine.eps)

The output electric field of the EO modulator in the spectral domain can be written as

$$E_{out}(\omega) = E_{in}(\omega) * T(\omega), \tag{4.17}$$

where $T(\omega)$ is the Fourier transform of Equation (4.15). Since $T(t)$ is a sinusoidal signal, $T(\omega)$ is simply two delta functions. The convolution of the input spectrum with delta functions simply means that the input spectral lines are shifted up by $\frac{\omega_r}{2}$ and down by the same amount, and then the two shifted results are summed together. Analytically, the Fourier transform of our field transfer function is

$$T(\omega) = \frac{m}{2}\frac{\pi V_m}{V_\pi}\left[\delta(\omega - \frac{1}{2}\omega_r) + \delta(\omega + \frac{1}{2}\omega_r)\right]e^{i\frac{1}{2}\omega_r\tau}. \tag{4.18}$$

Substituting Equations (4.18) and (4.6) into Equation (4.17), we obtain

$$E_{out}(\omega) = \left\{\sum_k E_k\delta[\omega - (\omega_o + \frac{2\pi k}{T_r})]\right\} * \left\{\frac{m}{2}\frac{\pi V_m}{V_\pi}\left[\delta(\omega - \frac{1}{2}\omega_r) + \delta(\omega + \frac{1}{2}\omega_r)\right]e^{i\frac{1}{2}\omega_r\tau}\right\} \tag{4.19}$$

$$= \frac{m}{2}\frac{\pi V_m}{V_\pi}\left[\sum_k E_k e^{i\frac{\omega_r}{2}\tau}\delta[\omega - \omega_o - (k-0.5)\omega_r] + \sum_k E_k e^{-i\frac{\omega_o}{2}\tau}\delta[\omega - \omega_o - (k+0.5)\omega_r]\right].$$

We can expand the summations in Equation (4.19)

$$\begin{aligned} E_{out}(\omega) = \frac{m}{2}\frac{\pi V_m}{V_\pi}\Big\{ &... + E_{k-1}e^{i\frac{\omega_r}{2}\tau}\delta[\omega - \omega_o - (k-1.5)\omega_r] \\ &+ E_{k-1}e^{-i\frac{\omega_r}{2}\tau}\delta[\omega - \omega_o - (k-0.5)\omega_r] \\ &+ E_k e^{i\frac{\omega_r}{2}\tau}\delta[\omega - \omega_o - (k-0.5)\omega_r] \\ &+ E_k e^{-i\frac{\omega_r}{2}\tau}\delta[\omega - \omega_o - (k+0.5)\omega_r] \\ &+ E_{k+1}e^{i\frac{\omega_r}{2}\tau}\delta[\omega - \omega_o - (k+0.5)\omega_r] \\ &+ E_{k+1}e^{-i\frac{\omega_r}{2}\tau}\delta[\omega - \omega_o - (k+1.5)\omega_r] + ...\Big\} \end{aligned} \tag{4.20}$$

It is clear that we can reorganize Equation (4.20) into a single summation

$$E_{out}(\omega) = \frac{m}{2}\frac{\pi V_m}{V_\pi}\sum_k B(k,\tau)\delta[\omega - \omega_o - (k-0.5)\omega_r], \tag{4.21}$$

where

$$B(k,\tau) = E_k e^{-i\frac{\omega_r}{2}\tau} + E_{k+1}e^{i\frac{\omega_r}{2}\tau}. \tag{4.22}$$

Recalling Equation (4.7), we can rewrite $B(k,\tau)$ as

$$B(k,\tau) = A_k e^{-i(\Phi_k + \frac{\omega_r}{2}\tau)} + A_{k+1}e^{-i(\Phi_{k+1} - \frac{\omega_r}{2}\tau)}. \tag{4.23}$$

We next wish to calculate the intensity and phase of E_{out}. The intensity is

$$I_{out} = |E_{out}|^2 = \left(\frac{\pi V_m}{2V_\pi}\right)^2 \sum_k C(k,\tau)\delta[\omega - \omega_o - (k-0.5)\omega_r], \tag{4.24}$$

where

$$C(k,\tau) = |B(k,\tau)|^2 = |A_k e^{-i(\Phi_k + \frac{\omega_r}{2}\tau)} + A_{k+1}e^{-i(\Phi_{k+1} - \frac{\omega_r}{2}\tau)}|^2. \tag{4.25}$$

Since m was only a phase term, it does not show up in the intensity equation. We proceed to simplify Equation (4.25) further.

$$\begin{aligned} |B(k,\tau)|^2 &= |A_k\cos(\Phi_k + \frac{\omega_r}{2}\tau) - iA_k\sin(\Phi_k + \frac{\omega_r}{2}\tau) \\ &\quad + A_{k+1}\cos(\Phi_{k+1} - \frac{\omega_r}{2}\tau) - iA_{k+1}\sin(\Phi_{k+1} - \frac{\omega_r}{2}\tau)|^2 \\ &= \left(A_k\cos(\Phi_k + \frac{\omega_r}{2}\tau) + A_{k+1}\cos(\Phi_{k+1} - \frac{\omega_r}{2}\tau)\right)^2 \\ &\quad + \left(A_k\sin(\Phi_k + \frac{\omega_r}{2}\tau) + A_{k+1}\sin(\Phi_{k+1} - \frac{\omega_r}{2}\tau)\right)^2. \end{aligned} \tag{4.26}$$

Multiplying out, we obtain

$$A_k^2\cos^2(\Phi_k+\frac{\omega_r}{2}\tau)+A_{k+1}^2\cos(\Phi_{k+1}-\frac{\omega_r}{2}\tau)+2A_kA_{k+1}\cos(\Phi_k+\frac{\omega_r}{2}\tau)\cos(\Phi_{k+1}-\frac{\omega_r}{2}\tau)$$
$$+A_k^2\sin^2(\Phi_k+\frac{\omega_r}{2}\tau)+A_{k+1}^2\sin(\Phi_{k+1}-\frac{\omega_r}{2}\tau)+2A_kA_{k+1}\sin(\Phi_k+\frac{\omega_r}{2}\tau)\sin(\Phi_{k+1}-\frac{\omega_r}{2}\tau). \tag{4.27}$$

If we regroup and simplify using trigonometric identities, we finally obtain

$$A_k^2+A_{k+1}^2+2A_kA_{k+1}\cos(\Phi_k+\frac{\omega_r}{2}\tau-(\Phi_{k+1}-\frac{\omega_r}{2}\tau))$$
$$=A_k^2+A_{k+1}^2+2A_kA_{k+1}\cos(\omega_r\tau+\Phi_k-\Phi_{k+1}). \tag{4.28}$$

We add a constant phase term $\omega_r\tau_o$ to provide a reference for our measurements:

$$C(k,\tau)=A_k^2+A_{k+1}^2+2A_kA_{k+1}\cos(\omega_r(\tau-\tau_o)+\Phi_k-\Phi_{k+1}). \tag{4.29}$$

Finally, we can factor out a negative sign from within the argument of the cosine function since cosine is a symmetric function.

$$C(k,\tau)=A_k^2+A_{k+1}^2+2A_kA_{k+1}\cos(\omega_r(\tau_o-\tau)+\Phi_{k+1}-\Phi_k). \tag{4.30}$$

The phase may also be calculated to be

$$\Phi_{out}(k,\tau)=\omega_r(\tau_o-\tau)+\Phi_{k+1}-\Phi_k. \tag{4.31}$$

We see then that I_{out} is the output spectral intensity, $C(k,\tau)$ is the intensity of the kth output spectral line, and $\Phi_{out}(k,\tau)$ is the spectral phase of the kth output spectral line. We also recall that Φ_{k+1} and Φ_k are the spectral phases of the $k+1$ and the kth

input spectral lines, respectively. Finally, A_k and A_{k+1} are the spectral intensities of the $k+1$ and the kth input spectral lines, respectively. The final equations are gathered together below for clarity:

$$E_{in}(\omega) = \sum_k E_k \delta[\omega - (\omega_o + \frac{2\pi k}{T_r})], \text{where} \tag{4.32}$$

$$E_k = A_k e^{-i\Phi_k} \tag{4.33}$$

$$I_{out} = |E_{out}|^2 = \left(\frac{\pi V_m}{2V_\pi}\right)^2 \sum_k C(k,\tau)\delta[\omega - \omega_o - (k-0.5)\omega_r], \text{where} \tag{4.34}$$

$$C(k,\tau) = A_k^2 + A_{k+1}^2 + 2A_k A_{k+1}\cos(\omega_r(\tau_o - \tau) + \Phi_{k+1} - \Phi_k) \tag{4.35}$$

$$\Phi_{out}(k,\tau) = \omega_r(\tau_o - \tau) + \Phi_{k+1} - \Phi_k. \tag{4.36}$$

An intuitive explanation of what is happening is that the spectral lines of the initial field $E_{in}(\omega)$ are mixed up and down to form the spectral lines of the output field $E_{out}(\omega)$. Each of the new spectral lines are formed from two adjacent initial spectral lines, and thus contain information about the relative phases between those the two initial spectral lines. By using a time-delay τ which adjusts how much of the power from a spectral line will mix up and how much will mix down, we can extract this phase difference between the initial spectral lines. Let us examine this process in more detail.

In order to completely characterize a pulse, we must measure the amplitude and phase of the original pulse train, $E_{in}(t)$. Using the spectral interferometric technique, we can obtain the amplitude and phase of the spectrum of the original pulse train $E_{in}(\omega)$. Complete characterization of the pulse's temporal amplitude and phase is obtained by performing a Fourier transform. From Equations (4.32)- (4.36), we see that in order to obtain the spectral intensity and phase of the original pulse, we

must extract A_k and Φ_k for all values of k. To do this, we first use the optical spectrum analyzer shown in Figure 4.1 to measure the output spectral intensity. An example of an output spectral intensity is shown in Figure 4.5, where the dotted lines represent the spectral lines arising from the modulation solid lines represent the original pulse train spectral lines. This gives us the ability to measure $C(k, \tau)$, which is the intensities for the kth modulation spectral lines (dotted lines).

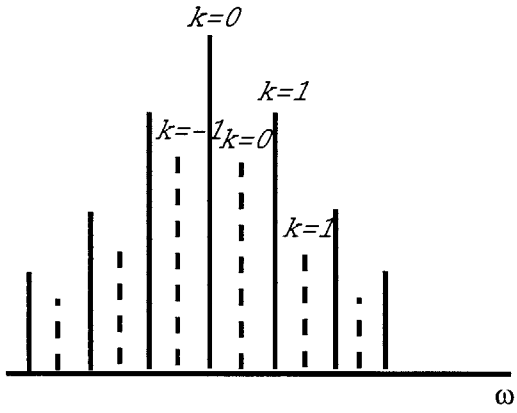

Figure 4.5: Diagram of an example output spectrum from the setup in Figure 4.1. The solid lines indicate the original pulse spectrum $E_{in}(\omega)$ and the dashed lines indicate the modulated pulse spectrum. (fig/outputdiagram.eps)

We first consider the definition of the reference phase $\omega_r \tau_o$. The definition of τ_o will correspond to a Φ_o, which we have chosen as our reference. If we assume a symmetric input pulse spectrum, one way of defining Φ_o is as the average of Φ_1 and Φ_{-1}. The time delay τ_o that corresponds to this is the τ measured when the modulated spectral lines $C(0, \tau)$ and $C(-1, \tau)$ are equal. Let us write the equations

for $C(0,\tau)$ and $C(-1,\tau)$ from Equation (4.35).

$$C(k=0,\tau) = A_o^2 + A_1^2 + 2A_o^2A_1^2\cos\left(\omega_r(\tau_o-\tau)+\Phi_1-\Phi_0\right) \tag{4.37}$$

$$C(k=-1,\tau) = A_{-1}^2 + A_o^2 + 2A_{-1}^2A_o^2\cos\left(\omega_r(\tau_o-\tau)+\Phi_o-\Phi_{-1}\right). \tag{4.38}$$

If we assume we have adjusted τ to τ_o and $C(0,\tau)$ is therefore equal to $C(-1,\tau)$, we can write

$$C(k=0,\tau_o) = C(k=-1,\tau_o) \tag{4.39}$$

and

$$A_o^2 + A_1^2 + 2A_o^2A_1^2\cos\left(\Phi_1-\Phi_o\right) = A_{-1}^2 + A_o^2 + 2A_{-1}^2A_o^2\cos\left(\Phi_o-\Phi_{-1}\right). \tag{4.40}$$

Since we have assumed a symmetric input spectrum, $A_1 = A_{-1}$, and Equation (4.40) becomes

$$\cos\left(\Phi_1-\Phi_o\right) = \cos\left(\Phi_o-\Phi_{-1}\right). \tag{4.41}$$

Solving for Φ_o, we see that

$$\Phi_o = \frac{\Phi_1+\Phi_{-1}}{2}. \tag{4.42}$$

However, we can also assume any reference phase we wish. We can also choose not to explicity choose a reference phase and simply obtain the phase within a constant unknown phase factor by disregarding $\omega_r\tau_o$ in our equations.

Next, we proceed to extract the spectral phase of another spectral line of our original pulse train. Let us find the phase $\Phi_{k=1}$. To do this, we first adjust τ until we see the $k = 0$ dotted line (representing the output spectral lines) in Figure 4.5 reach a maximum. At this point, we know that Equation (4.35) is

$$C(k = 0, \tau) = A_0^2 + A_1^2 + 2A_0A_1, \tag{4.43}$$

with

$$\cos(\omega_r(\tau_o - \tau) + \Phi_1 - \Phi_0) = 1 \tag{4.44}$$

We know the value of τ_o from measuring it earlier, and we also know the value of τ from having adjusted it to reach this point. Since ω_r is also known, we can solve for $\Phi_1 - \Phi_0$:

$$0, 2\pi, 4\pi, \cdots = \omega_r(\tau_o - \tau) + \Phi_1 - \Phi_0 \tag{4.45}$$

$$\Phi_1 - \Phi_0 = 0 - \omega_r(\tau_o - \tau). \tag{4.46}$$

Since we also know Φ_0 from having set that as our reference, we have therefore extracted the spectral phase of our initial field for $k = 1$. By repeating this process for all values of k, we can extract the spectral phase for every spectral line of $E_{in}(\omega)$. Finally, having obtained Φ_k for all k, we can use the Fourier Transform to calculate the temporal phase of our pulse.

There are several advantages to the use of spectral interferometry for the measurement of picosecond pulses. First of all, the resolution needed for measuring the

separate spectral lines is on the order of 0.01nm, which is achievable at the wavelengths being used (1550nm) more easily than at the second harmonic wavelengths (775nm). This resolution is based on the pulse width under investigation. Our interest lies in picosecond pulses, which have a bandwidth of roughly 1.5nm. As a result, we need a resolution of 0.01nm to give us a respectable 150 points for our measurement. Secondly, our high repetition rates (10GHz) and picosecond pulse lengths give us a reasonable number of spectral lines under the envelope (about 40 lines). This statement means that we will have a fairly accurate measurement of the chirp across a pulse. Finally, this interferometric method is non-iterative, and thus requires less processing than the previously discussed FROG method. However, one major challenge with this method is that the pulse-to-pulse coherency of the pulse train must be high. If the phase shifts from pulse to pulse, the resulting spectral lines are not stable enough for measurement. This limits us severely in the optical pulse sources we are able to use. Harmonically mode-locked fiber lasers do not have a high pulse-to-pulse coherency between adjacent pulses due to their construction. Instead, we must rely on injection controlled gain-switched DFB (distributed feedback) laser diodes or pulse-carving and compression.

Chapter 5

Pulse Characterization Experiment and Analysis

Both SHG FROG and the spectral interferometric method were investigated, though due to time and equipment constraints, the spectral interferometric method was the focus of this thesis. The setup for the spectral inteferometric method is shown again in Figure 5.1. We use an optical pulse source to generate a pulse train at a repetition

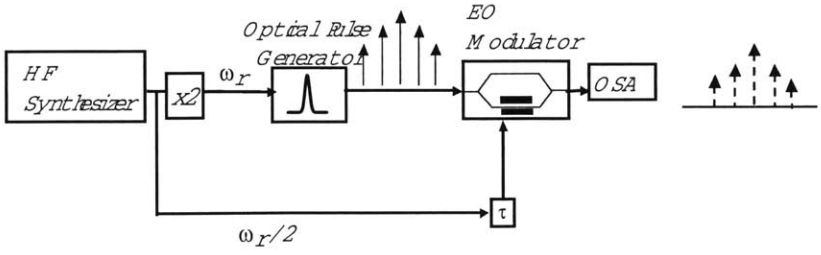

Figure 5.1: Setup for the spectral interferometric method of pulse characterization. (fig/specintsetup.eps)

rate ω_r. We then use an electro-optic modulator to modulate this pulse train with a sinusoidal modulation at half ω_r and include an adjustable RF time delay τ. As shown in the previous chapter, this time delay allows us to vary the power split in the modulated frequency lines due to spectral interference between the carrier frequency lines.

Let us first discuss the experimental setup for the characterization part of this experiment. We will discuss pulse sources in later sections of this chapter. The characterization experiment shown in Figure 5.1 relies on using an electro-optic modulator to modulate the pulse train of interest. We have developed the theory in Chapter 4 based on the use of a single-drive EO modulator. In this analysis, we assumed the modulation is applied only to a single arm of the modulator. In this configuration, the optical test signal experiences both phase-modulation as well as amplitude modulation. If our modulation is small, we can neglect this phase modulation. In Chapter 4, we assumed we can ignore this phase modulation based on our assumption that the RF drive voltage V_m will be less than $0.3V_\pi$. For operating conditions under which this assumption is not valid, a dual-drive modulator may be used. Dual-drive modulators apply only amplitude modulation to the input signal. With dual-drive modulators, both arms of the modulator are modulated an equal but opposite amount (Figure 5.2). For dual drive modulators, it is easy to see that only amplitude modulation will occur.

$$T_{\text{dual}}(t) = e^{i\phi(t)} + e^{-i(\phi(t)+V_b)}, \tag{5.1}$$

where V_b is a constant bias voltage. If we bias at the null, we obtain

$$T_{\text{dual}}(t) = e^{i\phi(t)} - e^{-i(\phi(t))} \tag{5.2}$$

$$= 2e^{i\frac{\pi}{2}} \sin(\phi(t)). \tag{5.3}$$

Thus, using a dual-drive modulator should increase the accuracy of our results, since pure amplitude modulation can be achieved without any undesired phase modulation.

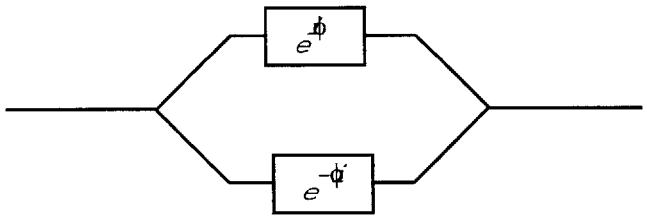

Figure 5.2: Diagram of a dual-drive modulator. Both arms are modulated an equal but opposite amount. (fig/emoddual.eps)

To calibrate a dual drive modulator such that the arms of the modulator are modulated exactly 180 degrees out of phase, we use a single synthesizer to generate the same modulation signal for both arms. Then, we put a phase delay on one arm of the modulator. With the modulation on, we can adjust the phase delay such that the modulation is balanced (symmetric). This corresponds to the arms of the dual-drive modulator being modulated exactly out of phase.

We also require a fairly accurate RF time-delay in order to adjust how the power in the carrier frequency lines are split into the modulated frequency lines. We use a phase delay to which we attach an accurate micrometer in order to read off the

length changes. The lengths we read off this micrometer can be directly converted to a corresponding phase shift. In order to calibrate this RF time delay, we can build a simple interferometer with one arm containing the RF time delay and the other arm simply containing a length of RF cable (Figure 5.3a). We then pass the two arms into a mixer and measure the voltage. By adjusting the time delay until we read the minimum voltage and then adjusting the time delay until we read the maximum voltage, we can find how the phase shift of the time delay corresponds to the length reading of the micrometer. Another method is to use the signal into the RF time delay to trigger a fast sampling oscilloscope, and observing the signal out of the RF time delay on the oscilloscope (Figure 5.3b). Using both methods, we verified that each mil of the time delay corresponds to one radian of phase shift at 10GHz with an error of $+/-0.02$ radians.

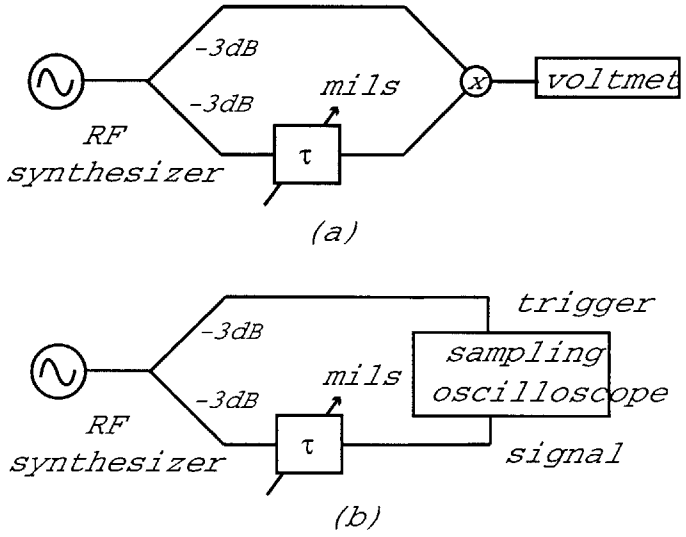

Figure 5.3: Experimental setup for interferometric characterization of the RF time delay. Diagram (a) shows the voltage amplitude technique and diagram (b) shows the phase measurement method. (fig/rfinter.eps)

The final piece of equipment shown in Figure (5.1) is a high-resolution optical spectrum analyzer. The resolution needed for the spectrum analyzer depends mainly on the repetition rate of the pulse train of interest. A repetition rate of 20GHz corresponds to spectral line spacings of 20GHz, or 0.16nm. If the resolution of our optical spectrum analyzer is 0.01nm, we obtain 16 points for each spectral line. The bandwidth of our pulse train divided by the repetition rate of the pulse train determines the number of spectral lines we see. A pulse train of 2ps FWHM pulses corresponds to a bandwidth of 221GHz, or 1.77nm. For a 20GHz repetition rate, this means we will see approximately 10 spectral lines. If we decrease our repetition rate to 10GHz, we will see approximately 20 spectral lines.

5.1 Measurement Methodology

We have developed two methods to gather data for this characterization technique. The first was described at the end of Chapter 4. Using this method, we first minimize the output spectral line of interest ($C(k,\tau)$) and measure the time delay corresponding to that point. We then maximize the line of interest and measure the time delay corresponding to that point. Each of these points should give us a measurement of $\Phi_{k+1} - \Phi_k$. We can repeat this for each of the k lines in the output spectral intensity. The second method involves adjusting τ to a known location and then saving the output spectrum at that particular τ. We repeat this for several measurements of τ (in this particular case, we used 13 measurements). Then, we use a fitting program to fit each of the k spectral lines to the expected behavior. This technique should result in a more accurate measurement and give us a much clearer estimation of the error in the measurement. Furthermore, as the spectral lines increase or as we analyze

shorter and shorter pulses, it becomes more and more difficult and time-consuming to measure each spectral line by hand. A fitting program allows us to quickly arrive at a measurement of the phase.

5.2 Verification and Calibration

We first wish to examine this pulse characterization method using the simplest pulse source available, in order to verify that the method works and to calibrate our setup. When we have verified that the method works as we expect, we can then move on to examine other optical pulse sources which are more applicable to real-world communication networks.

5.2.1 Simple Optical Pulse Source

We choose to use a continuous wave (CW) source amplitude modulated at 20GHz to obtain a sinusoid on top of the carrier freuqency. We then use the spectral interferometric method to measure the phase of this sinusoid (within a constant phase factor). Then, we insert a length of fiber after our pulse source. The group velocity dispersion effects from this length of fiber should cause a phase shift between the different modes of the sinusoid which should be observable with our method. Figure 5.4 shows the experimental setup for generating the sinusoid.

Let us examine our amplitude modulated input test signal. We have CW light at 1552nm passing through an EO modulator which is modulated at 20GHz while biased at quadrature. At quadrature, the small signal response of the amplitude modulator is linear. Thus, in the time domain, we have a carrier at frequency ω_o on top of a

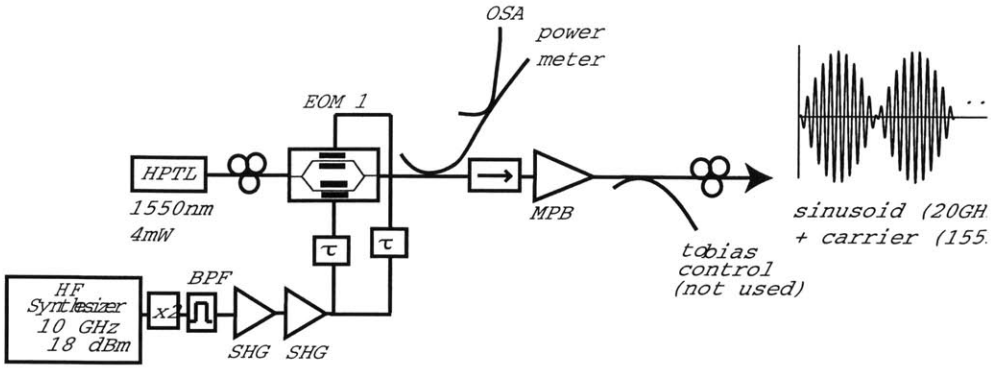

Figure 5.4: Setup for the generation of a sinusoid modulated wave on top of a carrier. HPTL is an HP tunable laser, OSA is the optical spectrum analyzer, BPF is a bandpass filter, and EOM is the electro-optic modulator.
(fig/sinesource.eps)

sinusoid at the modulation frequency ω_r:

$$\begin{aligned} E_{in}(t) &= e^{-i\omega_o t}(1 + cos(\omega_r t)) \\ &= e^{-i\omega_o t}(1 + e^{i\omega_r t} + e^{-i\omega_r t}) \\ &= e^{-i\omega_o t} + e^{-i(\omega_o - \omega_r)t} + e^{-i(\omega_o + \omega_r)t}. \end{aligned} \tag{5.4}$$

Propagation through fiber is determined by the propagation constant β, which is frequency dependent. From Chapter 2, we recall that we can expand β in a Taylor series

$$\beta(\omega) = \beta_o + \beta_1(\omega - \omega_o) + \frac{1}{2}\beta_2(\omega - \omega_o)^2 + ... \tag{5.5}$$

As a wave is propagated through fiber of length L, each frequency ω is multiplied by $e^{i\beta(\omega)L}$. For our input pulse train, we have three frequency components: one at ω_o,

one at $\omega_o + \omega_r$ and one at $\omega_o - \omega_r$ (Figure 5.5). Thus, as this wave propagates down a length of fiber L, it becomes

$$E_p(t) = e^{i(\beta_o L - \omega_o t)} + e^{i(\beta_o L - \beta_1 \omega_r L + \frac{1}{2}\beta_2 \omega_r^2 L) - i(\omega_o - \omega_r)t} + e^{i(\beta_o L + \beta_1 \omega_r L + \frac{1}{2}\beta_2 \omega_r^2 L) - i(\omega_o + \omega_r)t}. \tag{5.6}$$

We can pull out the common term $e^{i(\beta_o L)}$:

$$E_p(t) = e^{i(\beta_o L)} \left(e^{-i\omega_o t} + e^{i(-\beta_1 \omega_r L + \frac{1}{2}\beta_2 \omega_r^2 L) - i(\omega_o - \omega_r)t} + e^{i(\beta_1 \omega_r L + \frac{1}{2}\beta_2 \omega_r^2 L) - i(\omega_o + \omega_r)t} \right). \tag{5.7}$$

Let us take a look at the phases of the separate frequency lines. The frequency line at $\omega_o + \omega_r$ is our $k = 1$ line, and the frequency line at $\omega_o - \omega_r$ is our $k = -1$ line. Thus, the phase of our $k = 1$ line should be

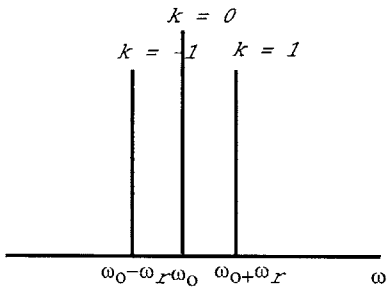

Figure 5.5: Spectrum of our sinusoidally modulated wave. The modulator is biased at quadrature. The modulation frequency is ω_r and the carrier frequency is ω_o. (fig/sinespec.eps)

$$\Phi_{k=1} = \beta_o L + \beta_1 \omega_r L + \frac{1}{2}\beta_2 \omega_r^2 L, \tag{5.8}$$

and the phase of our $k = -1$ line should be

$$\Phi_{k=-1} = \beta_o L - \beta_1 \omega_r L + \frac{1}{2}\beta_2 \omega_r^2 L, \tag{5.9}$$

and the phase of our $k = 0$ line should be

$$\Phi_{k=0} = \beta_o L. \tag{5.10}$$

Figure 5.6 shows the measured optical spectrum of the amplitude modulated input wave. Note that more than three spectral lines are present. The unexpected presence of seven spectral lines is due to the fact that we are driving the amplitude modulator into the nonlinear regime with a 23dBm large amplitude RF input power. In this experiment, we will ignore these extra spectral lines, since they will not impact the measurement and we wish to consider the simplest situation possible in order to verify the correct operation of the spectral interferometric measurement method.

5.2.2 Pulse Characterization Experiment

Let us now consider what occurs when this optical wave passes through the spectral interferometry electro optic modulator (EOM2 as shown in Figure 5.1. The full setup of the sinusoidal characterization mesurement is shown in Figure 5.7. According to Chapter 4, we should obtain a modulated pulse spectrum with intensities corresponding to

$$\begin{aligned} C(k,\tau) &= A_k^2 + A_{k+1}^2 + 2A_k A_{k+1} cos(\Phi_{k+1} - \Phi_k + \omega_r \tau_o - \omega_r \tau) \\ &= A_k^2 + A_{k+1}^2 + 2A_k A_{k+1} cos(d\Phi_{k+1,k} + \omega_r \tau_o - \omega_r \tau). \end{aligned} \tag{5.11}$$

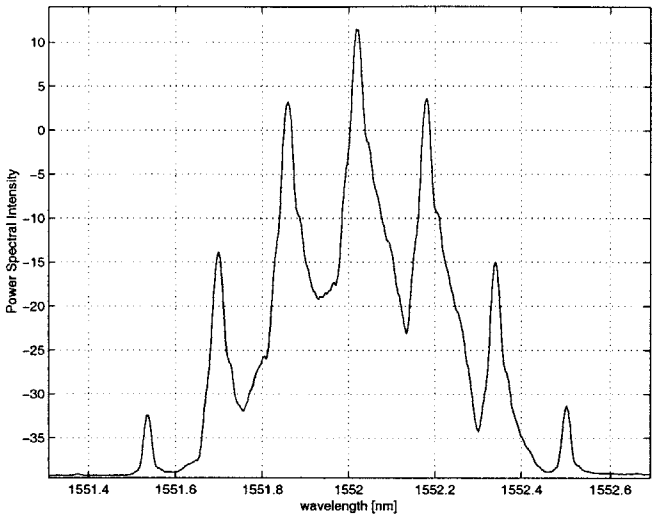

Figure 5.6: Optical pulse spectrum taken immediately before the fiber length. (fig/sineinputspec.eps)

where τ_o is simply a reference time delay setting. Thus, the phase difference between $C(k=0,\tau)$ and $C(k=-1,\tau)$ is given by

$$\begin{aligned} d\Phi_1 - d\Phi_0 &= (\Phi_1 - \Phi_0) - (\Phi_0 - \Phi_{-1}) \\ &= (\beta_1\omega_r L + \frac{1}{2}\beta_2\omega_r^2 L) - (\beta_1\omega_r L - \frac{1}{2}\beta_2\omega_r^2 L) \\ &= \beta_2\omega_r^2 L. \end{aligned} \tag{5.12}$$

Let us now consider the length of fiber necessary to add a π phase shift to the phase difference between the two modulated lines $C(k=0,\tau)$ and $C(k=-1,\tau)$. We know that for single-mode fiber, β_2 is approximately $20\text{ps}^2/\text{km}$. We also know that our modulation frequency ω_r is $2\pi \times 20\text{GHz}$. This corresponds to .126rad/ps. We wish

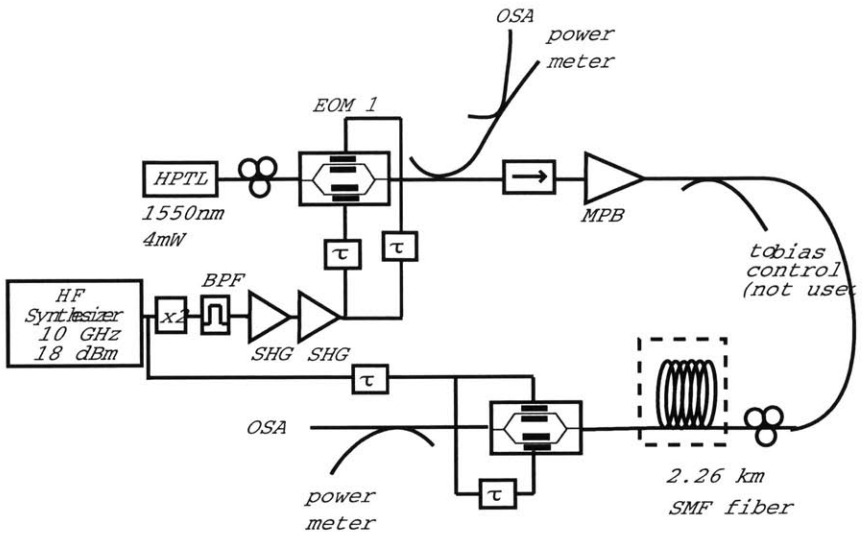

Figure 5.7: Setup for the characterization of a sinusoidally modulated wave on top of a carrier. We will characterize this source both with and without the length of fiber. (fig/sinesetup.eps)

to solve Equation (5.12) for L.

$$\pi = \beta_2 \omega_r^2 L \tag{5.13}$$

$$L = 9.9472\text{km}.$$

Thus, we need about 9.9472km of fiber to add a π phase shift to the $k = 0$ and $k = -1$ modulated intensity lines. It is interesting to note that the phase shift between the two modulated intensity lines depends only on the group velocity dispersion and is independent of the dispersion.

We first observe the output modulated spectrum without the long SMF spool shown in Figure 5.7. As expected, when we vary τ, the amplitudes of the two modulated spectral lines $C(k = 0, \tau)$ and $C(k = -1, \tau)$ vary together. This measurement

implies that in the absence of a long fiber span in the system, there is zero phase shift between the $k = -1$ and $k = 0$ frequency lines. This result is expected since without a significant amount of fiber, the group velocity dispersion-length product ($\beta_2 L$) termin Equation (5.13) is quite small. The intensities of the spectral lines shown in Figure 5.5 also seem to be fairly stable. Figure 5.8 shows a plot of the spectrally interfered frequency components present at the output of EOM2 in Figure 5.7 without additional fiber in the setup. Note that the amplutude modulated spectral components present at the input of EOM2 have been nulled out fairly well, and that significant insertion loss is suffered through this modulator as a result of biasing at the null. We take data both by hand and also using the fitting program we developed

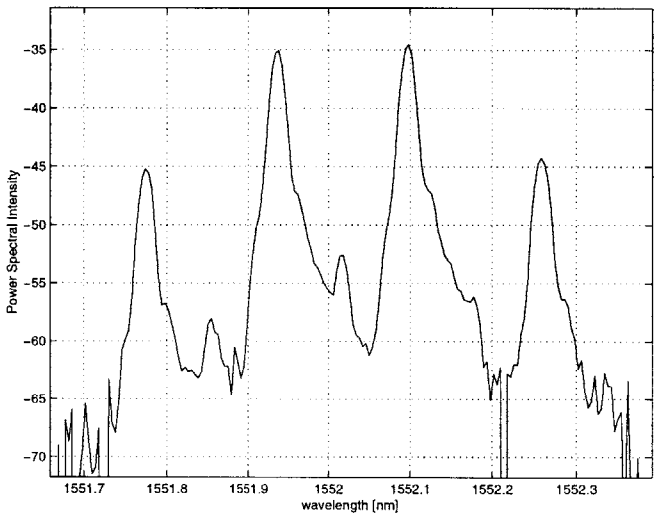

Figure 5.8: Power spectral intensity plot of the output spectrum, with no additional spool of fiber. $\omega_r \tau$ corresponds to approximately 2 radians for this plot. (fig/outnofiber.eps)

in Section 5.1. Taking the data by hand, we find that for our $k = -1$ line, the minimum spectral intensity occured when the RF time delay was set at 2.97mils and the

maximum occured at when the RF time delay was set at 4.65mils. These micrometer readings correspond to 5.94 radians and 9.3 radians at 20GHz, respectively. We solve for $\Phi_0 - \Phi_{-1}$ and find that it is about -6.05 radians. For our $k = 0$ line, we find that the minimum spectral intensity occured when the RF time delay was set at 2.94 mils and the maximum occured at 4.63 mils. These measurements correspond to a $\Phi_1 - \Phi_0$ of -6.00 radians. We note that as expected, the $k = 0$ line and the $k = -1$ line are in phase when the long 2.26km SMF span is not included in the experimental measurement system shown in Figure 5.7.

Taking the data using the fitting program described in Section 5.1, we find the difference between the phase of our $k = 0$ line and our $k = -1$ line to be 0.155 radians. To obtain this value, we first took 12 traces of the spectral intensity. Each trace corresponded to a certain RF time delay measurement τ and were taken at intervals of $\tau = 0.5$mils from 0.00mils to 6.00mils. From each trace, we then extracted the intensity of both the $k = -1$ line and the $k = 0$ line. We fit these data points to the cosine function as given in Equation (5.11). This measurement differs from our hand measurements of 0.05 radians by only 0.1 radians. This is within the error of finding the minimum or maximum by hand. Figures 5.9 shows the fits for the $k = -1$ line and the $k = 0$ line.

We next observe the output spectrum with 2.26km of fiber in the system. If a π phase shift between the $k = -1$ and $k = 0$ spectral components of our output corresponds to 9.95km of fiber as shown in Equation (5.13), then 2.26km of fiber should give us a $\pi/4.4$ phase shift. Figure 5.10 shows a plot of the modulated spectrum with 2.26km of fiber in the system at $\omega_r\tau = 2$rad. Taking the data by hand, we find that for our $k = -1$ line, the minimum intensity occured at 3.04mils and the maximum occured at 4.76mils. The minimum and the maximum time delay readings correspond

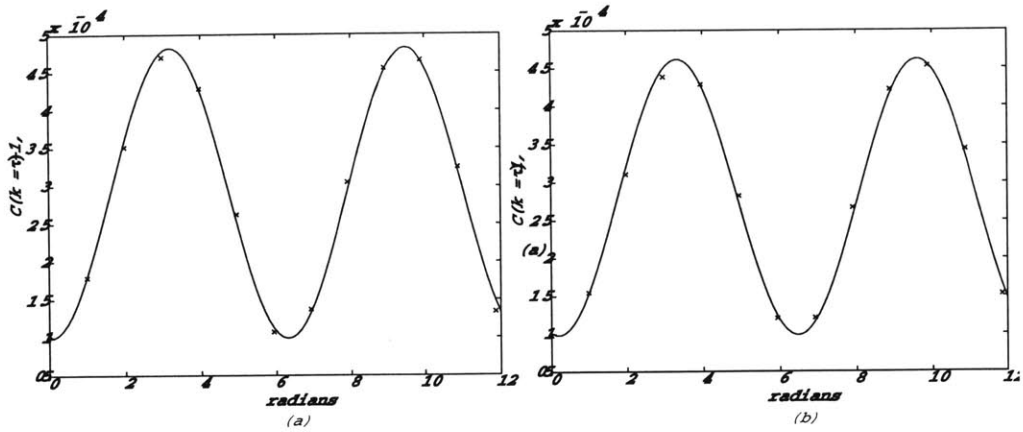

Figure 5.9: Plot of (a) $C(k=-1,\tau)$ and (b) $C(k=0,\tau)$ taken of the setup with no additional fiber. The solid line is the fit and the crosses are the data points. (fig/nofiberfit.eps)

to 6.08 radians and 9.52 radians at 20GHz, respectively. We solve for $\Phi_0 - \Phi_{-1}$ using the experimentally measured parameters in Equation (5.11) and find that it is about -6.23 radians. For our $k=0$ line, we find that the intensity minimum occured at 2.39 mils and the maximum occured at 3.92 mils. This result corresponds to a $\Phi_1 - \Phi_0$ of -4.74 radians at 20GHz. This indicates that the phase difference between the two modulated spectral lines is about 1.49 radians. The phase difference between the $k=-1$ and $k=0$ components measured by hand for the experimental setup without the 2.26km of SMF fiber was about 0.05. We expect the phase difference between the setup with fiber and the setup without fiber to be near $\pi/4.4$. The difference we measured by hand is 1.44 radians, which is about twice what we expected. Such an error is most likely due to the bias drift in the spectral interferometry modulator. Hand measurements are affected more by this drift than measurements taken with the fitting program, since the length of time needed to take the measurements accurately by hand is much longer than that needed to take the measurements using the program.

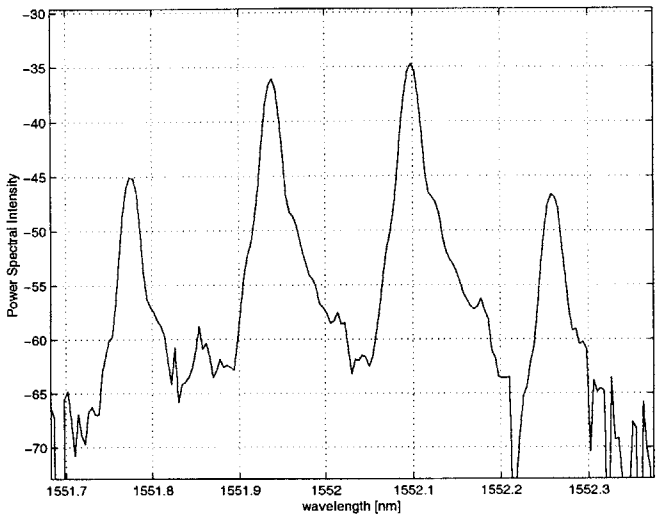

Figure 5.10: Power spectral intensity plot of the output spectrum, with 2.26km of fiber in the system. $\omega_r\tau$ corresponds to approximately 2 radians for this plot. (fig/outfiber.eps)

Taking the data using the fitting program as described in Section 5.1, we find the difference between the phase of our $k = 0$ line and our $k = -1$ line to be about 0.789 radians. This differs from our hand calculation by about .701 radians, which corresponds to about 0.35 mils. This is within the error of our hand calculation since a small drift in the bias of the spectral interferometry modulator can affect the location of the maximum and minimum of our spectral lines. We also expect the difference between the phase calculated for the setup with the fiber and the setup without the fiber to differ by roughly $\pi/4.4$. We obtain a difference of 0.633, which differs from the expected value of 0.714 by 0.08 radians. This difference corresponds to 0.04 mils, which is within the error of our measurement. Our experiment, when measured using our data fitting program, coincides well with theory. Figures 5.11 shows the fits for the $k = -1$ line and the $k = 0$ line.

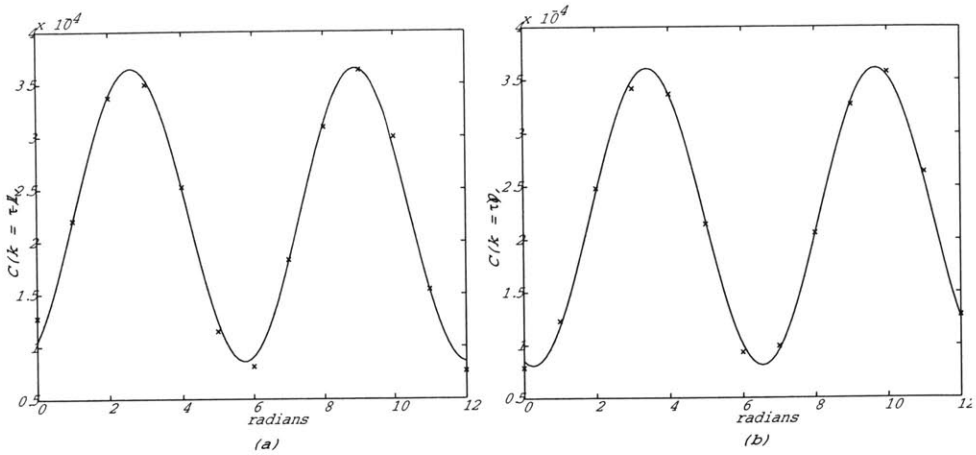

Figure 5.11: Plot of (a) $C(k = -1, \tau)$ and (b) $C(k = 0, \tau)$ taken of the setup with 2.6km additional fiber. The solid line is the fit and the crosses are the data points. (fig/fiberfit.eps)

We also observed a 10km fiber spool in the system. It was fairly clear that the modulated lines were about a π phase shift from each other. This π phase shift remained relatively constant throughout the experiment. However, the spectral intensity of both modes was varying significantly over short periods of time, making it impossible to take useful data using either hand measurements or our data fitting program. This variation affected the intensity of both modes equally. Thus, the π phase shift remained constant. This suggests the fast variation of the spectral intensity was due to variation in $\omega_r \beta_1 L$ with time. We know that the index of fiber varies at about 1.1×10^{-5} per degree Celcius. If our length is 1km, this corresponds to a phase variation of about 4.6 radians. If our length is 10km, a variation of even a tenth of a degree Celcius will give us a phase variation of about 4.6 radians - almost a 2π phase shift. The temperature variations in the 10km spool do account for the significant variation in the phase across both modes of our input pulse.

5.3 Practical Optical Pulse Sources

Let us now consider the application of this spectral interferometric pulse characterization method to practical optical pulse sources as may be used in communication networks. We observed the behavior of several optical pulse sources. First, a harmonically mode-locked fiber laser was used as a short pulse source (Figure 5.12). The laser produced 2ps pulses with a 12.5GHz repetition rate at a center wavelength of 1550nm. When observed with a high-resolution optical spectrum analyzer, however, it was found that the spectrum of this harmonically mode-locked laser was not stable in intensity over even short periods of time. We believe this instability in the optical spectrum is due to a lack of pulse-to-pulse coherency. In the harmonically mode-locked laser we used, there are 34,060 pulses in the fiber ring at any one time. Each pulse in the cavity experiences a slightly different phase and amplitude modulation due to the active harmonic mode-locking process in the fiber. As a result, every 34,060th pulse may be fairly similar, but the adjacent pulses at the output of the fiber laser are not. The optical spectrum analyzer averages the pulse train and this averaged pulse train spectrum we observe exhibits significant intensity variations due to the phase differences between adjacent pulses in the pulse train. For our measurements to work, we need a source with a stable spectrum, such that when we amplitude modulate the spectrum, we can make accurate measurements of the intensities of the spectral lines.

To solve this spectral instability problem, we used a DFB (distributed feedback) laser diode which emitts continuous wave (CW) light and an electro-optic modulator pulse carver. Since we are applying amplitude modulation to a CW laser, the pulse-to-pulse coherency should be high, and the spectrum should be fairly stable. Typical

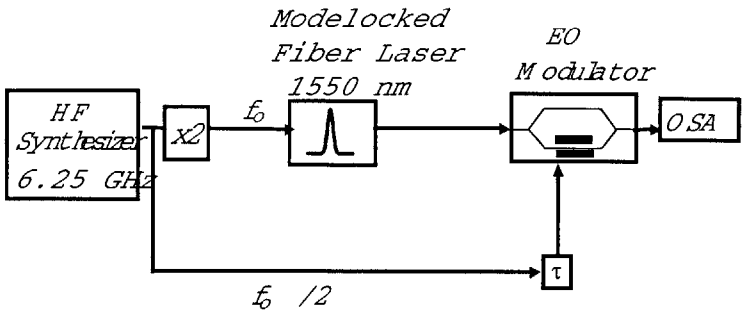

Figure 5.12: Setup for the spectral interferometric method of pulse characterization using harmonically mode-locked fiber laser at 1550nm. (fig/specintsetup1.eps)

DFB linewidths are on the order of $10 - 100$MHz.[30] This corresponds to a coherence lengths of 31ns to 3.1ns, where we have arrived at a rough estimate of coherence length by dividing $2/\Delta\omega$. Figure 5.13 shows the setup for this experiment. We drive the modulator with a 20GHz sinusoidal RF input such that we obtain 30ps pulses at a repetition rate of 20GHz. Since this pulse source will only give us a few spectral lines (due to the sinusoidal nature of the modulation), we wish to compress the pulses and thus generate more spectral lines to further evaluate spectral interferometry as a pulse characterization technique. This compression is done through the interaction of self-phase modulation (SPM) and group-velocity dispersion as the pulse propagates through a length of fiber with a given optical power. In our case, this pulse compressor first amplifies our signal and then passes it through approximately one kilometer of dispersion decreasing fiber to compress the pulses. Such compression is referred to as soliton compression. For more details on soliton effect compression, please refer to Agrawal, Section 6.4.[15] After compression, this pulse train provides additional spectral lines with which to perform the spectral interferometric measurement.

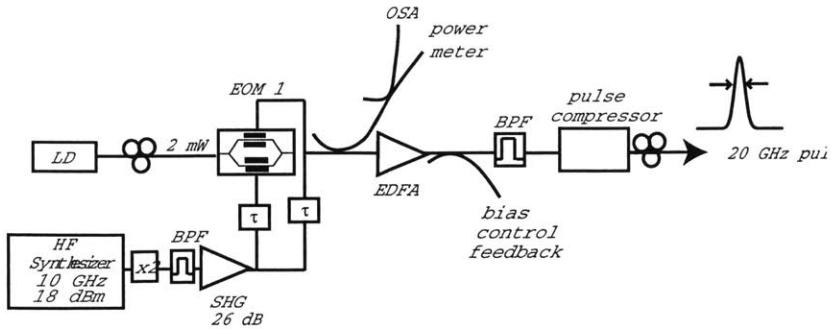

Figure 5.13: Setup using pulse carving to obtain high pulse-to-pulse coherency. LD is the laser diode that outputs CW at 1552nm, EOM stands for electro-optic modulator, and the bias control feedback is used to maintain the EOM bias at the null. The EDFA is an erbium-doped fiber amplifier and is necessary to saturate the pulse compressor. (fig/specintsetup2.eps)

We first perform this experiment with the pulse carving modulator biased at the null. The output of the pulse carver modulator will still be approximately 30ps FWHM pulses at a repetition rate of 20GHz, but there will be an amplitude modulation on top of the pulses corresponding to 40GHz from our bias at the null. The amplitude modulation should be small, since we are unable to increase the modulation depth more than about 5dB because we are biasing the modulator at the null. At the input to our pulse carver, the RF modulation power is only 0dBm. The bias of the pulse carver modulator walks off fairly quickly, so we use a bias control circuit to maintain the bias. This bias control circuit adds a low frequency (1kHz) and low amplitude ($10\text{mV}_{\text{p-p}}$) dither to our modulation signal. Using the modulator bias control circuit, we see that the performance of the pulse carver modulator is improved because the amplitude variation of the spectral lines at the output of the pulse carver is reduced to $2\% - 5\%$ of the spectral line amplitude.

This signal is next amplified by an erbium-doped fiber amplifier (EDFA) in or-

der to saturate the amplifier within the pulse compressor. We include a bandpass filter between the amplifier and pulse compressor to reduce the ASE (amplified spontaneous emission) from the amplifier. Observing the output of the EDFA, we find that variation in the spectral lines has increased to $10\% - 15\%$ of the spectral line amplitude. This variation is most likely due to the interaction of the dither on the bias circuit with the EDFA. The next stage is the pulse compressor, which amplifies our signal and then passes it through 1km of dispersion decreasing fiber to compress the pulse. We did not model the effect of this pulse compressor on our signal. We observe the output of our pulse compressor to include roughly twice the number of lines at the input. We see 7 spectral lines at the output of this pulse compressor. Next, we proceed to use this spectral interferometric method to analyze this pulse train. The setup for this characterization is similar to that shown in Figure 5.7. We bias the spectral interferometry modulator EOM2 at a null and modulate it at 10GHz with an adjustable RF phase delay. We use the same modulator as we used with the calibration experiment, but we drive only one arm. Thus, this data is for the single arm modulation case. We do not use a bias circuit for this second modulator since the dither on the modulation may affect the measurement. Figure 5.14 shows the setup for this experiment.

Observing the output of the second modulator, we see that the undesired variation of the spectral intensities is still about $10\% - 15\%$. The bias of the second modulator also has a tendency to drift in about a 5 minute time period. Furthermore, it seems that certain carriers seem to have a greater variation in intensity than other carriers. We take twelve traces of the optical spectrum analyzer, at τ set at 0.5 mil intervals. When we attempt to fit this data, however, it is clear that the fit is not very accurate. A plot of the output spectral intensity is shown in Figure 5.15. The data and fits for

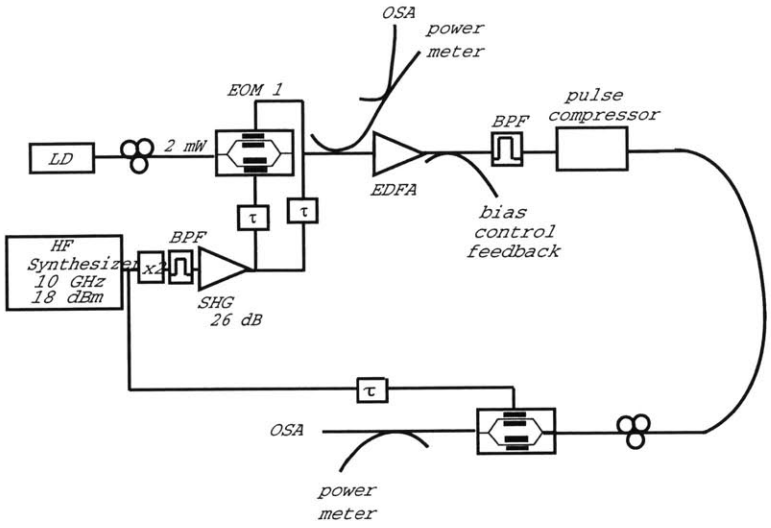

Figure 5.14: Setup for the characterization using spectral interferometry for the pulse carved and compressed pulse source. (fig/nullsinglesetup.eps)

the $k = -2$ line and the $k = 0$ line are shown in Figure 5.16.

Several significant sources of error exist in this measurement. First of all, the bias for our spectral interferometry modulator EOM2 in Figure 5.14 modulation varies over the course of our measurement. This detriment can be seen in the variation of the carrier frequency intensities over the set of spectral intensity plots we collected. However, in examining the behavior of the carrier spectral lines, it is clear that some of the spectral lines are varying more than others. This suggests something more than a simple bias control issue is occuring.

Another possibility is that the temperature fluctuation from the fiber in our system is producing a fluctuating phase shift. Recall from the previous section our calculation of the effect of temperature variation on the phase of a pulse propagating through fiber. We calculated that a temperature change of one degree Celcius can

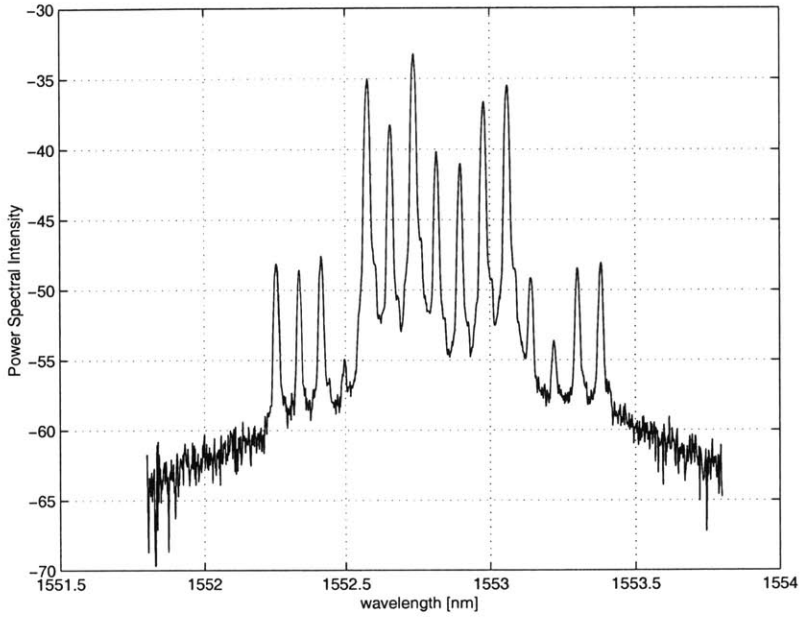

Figure 5.15: Plot of output spectral intensity after passing through the second modulator, for when τ is set at about 1mil or 2radians. (fig/nullsingleout.eps)

lead to as much as a 1.5π phase shift on a pulse train passing through a kilometer of fiber. The pulse compressor we use in this setup contains roughly 1km of fiber and is not temperature controlled. The process of compression through this dispersion decreasing fiber is probably causing temperature changes which will alter the phase of our pulse train of interest. If the temperature of this fiber fluctuates, the phase of our pulse train will also fluctuate, which can account for some of the effects we see in the modulated spectrum.

A third possible cause of error is that we are also driving the pulse characterization modulator on only one arm, and we may be causing a significant phase modulation as well as an amplitude modulation. However, we found that switching to a dual-drive modulator did not improve the performance of the system. This corresponds well

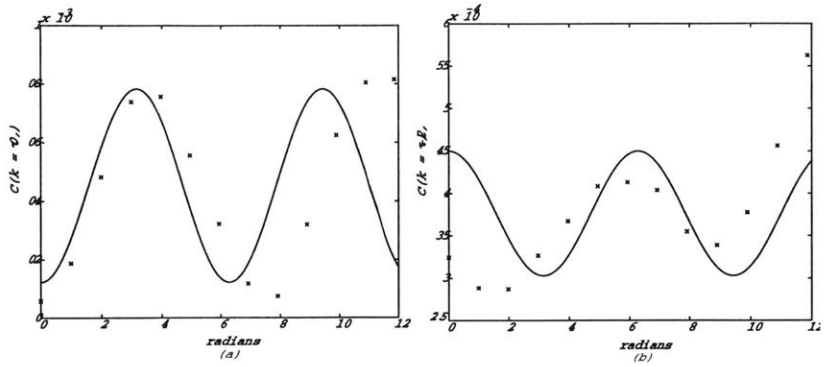

Figure 5.16: (a) shows the fit (solid line) and the data (crosses) for the $k = 0$ line of the output spectrum $C(k, \tau)$. (b) shows the fit (solid line) and the data (crosses) for the $k = -2$ line of the output spectrum. (fig/fitnulldata.eps)

to theory, since we were only driving the modulator at about 3.6dBm, which is well below the V_π of this modulator. (The modulator V_π is about 5V.)

From this analysis, it seems most likely that the temperature fluctuations in the kilometer length of fiber was causing phase fluctuations in our pulse of interest and making it impossible to measure the phase of our pulse train. It seems clear from these experiments that this pulse characterization method has several disadvantages which may make it rather impractical for use in actual communication networks.

Chapter 6

Conclusions and Future Work

The development of shorter and shorter optical pulses for a variety of practical applications indicates a need for a robust method of optical pulse characterization. One such application is that of optical communication networks. Most communication networks in use today are wavelength division multiplexing (WDM) networks. However, optical time-division multiplexing (OTDM) networks have a variety of advantages over WDM networks if several difficulties related to short optical pulse transmission can be overcome. These difficulties include noise accumulation, group velocity dispersion, polarization dispersion, and material nonlinearities. Investigation and control of such effects requires a robust and accurate method of measuring short pulses. Typical pulse length in OTDM systems is a few picoseconds in length, and thus we are interested in methods for accurately characterizing picosecond pulses.

We have investigated several methods of optical pulse characterization in this thesis. We have shown that using only the optical autocorrelation and spectrum of a pulse is insufficient to derive complete information about the phase or chirp of a pulse.

We next investigated the various frequency-resolved optical gating (FROG) methods, which were originally developed for femtosecond optical pulses. The challenges of adapting the FROG technique to characterize picosecond pulses lies in the fact that picosecond pulses have a much smaller bandwidth than femtosecond pulses, thus making it difficult to acquire the resolution necessary for the FROG technique. Finally, we investigated the spectral interferometric technique as presented by Debeau.[7] This technique is designed for characterization of picosecond pulse lengths and uses common fiber-coupled equipment, making it simple to build and test. Furthermore, it provides for a direct calculation of the phase, while the FROG method requires an iterative algorithm. We have focused mainly on testing and characterizing this third method due to time and equipment constraints.

Careful investigation of this third technique has revealed several disadvantages. First of all, this method only works for a pulse source which has a high pulse-to-pulse coherency. If the phase of the pulses in the pulse train varies from one pulse to the next, we are unable to make any measurements. This is due to the fact that we are interfering the spectral lines with each other. Significant phase variations over short periods of time will show up as significant variations in the spectral intensities of the interference spectrum, thus making it impossible to measure consistent data from one moment to the next. Secondly, the method is sensitive to temperature changes. If we propagate a pulse train with high pulse-to-pulse coherency through a significant amount of fiber, temperature fluctuations of the fiber can also cause a significant phase variation in our interfered spectrum. Both of these effects arise from the fact that we are interfering the spectral lines of our pulse train with each other. This interference will increase the sensitivity of our measurement to fluctuations in the phase of our pulse train. For this measurement to work, we will need a pulse source

with a high pulse-to-pulse coherency. Furthermore, we cannot propagate this pulse through significant lengths of fiber without temperature control of the fiber lengths, as that will cause fluctuations in the phase of the input spectral pulses. As a result, it does not seem likely that this method will be useful for practical measurements of pulses in optical communication networks.

However, there are several advantages to this method that can prove useful should we need to characterize a well-behaved pulse source. First of all, the phase of a pulse train can be determined in a direct manner without resorting to iterative algorithms. Secondly, the setup is simple and consists of common fiber-coupled equipment, making it easy to use. These advantages indicate that for characterizing well-behaved pulse sources, the spectral interferometric pulse characterization method is superior to the FROG method.

Future work should include continuing the investigation of pulse characterization methods, in particular, the investigation of applying the FROG method to picosecond pulses.

Appendix A

Matlab Code for Fitting Spectral Interferometric Data

```
function [Alin,C1,C2,dPhi, fvals] = phasecalc(P0, w0,
wpulse,specpulse, wall, pulseall, mils)
% This should derive the phase of the frequency components
% Inputs: P0 is the power vector (column) for nonmodulated line
      % wall is the matrix of w vectors.  Each row corresponds
      %   to a tau measurement.  should be wall(tau,spectrum)
      % pulseall is the matrix of spectrum measurements.  Each row
      %   corresponds to a a tau measurement
      % mils is the tau measurmeent in mils

% First, we want to find the amplitudes of each of the k lines
N = 3; % N is the # of spectral lines; this should be odd.
[A,fi,f] = findA(wpulse,w0,specpulse,P0,N,20);
Alin = 10.^(A/10);  % For dB

% We next want to find the peaks of the modulated spectral lines
Nmod = 7;
[ma, na] = size(wall);
Ck = zeros(ma,Nmod);
fk = zeros(ma,Nmod);
freq = zeros(ma, na);
for ii = 1:ma
    [Ck(ii,:),fk(ii,:),freq(ii,:)] =
    findA(wall(ii,:)',w0,pulseall(ii,:)',P0,Nmod,10);
end;
```

```
Cklin = 10.^(Ck./10);

% We also manually record the micrometer settings for each plot,
% and transform that to a phase tau
tau = 2*mils;

modlines = (Nmod+1)/2 -2;
center = (Nmod+1)/2;
Cknorm = Cklin;
C1 = zeros(1,modlines);
C2 = zeros(1,modlines);
dPhi = zeros(1,modlines);
fvals = zeros(1,modlines);

for ii = 1:(modlines)
    xguess = [0 1 0];
    k = ii*2+1;
    [x, fval] =
    fminsearch('cktau3',xguess,optimset('MaxFunEval',30000,...
      'MaxIter',10000,'TolFun', 10^-12,'TolX',10^-12,...
      'Display','iter'),tau,Cknorm(:,k)');
    fvals(ii) = fval;
    C1(ii) = x(1);
    C2(ii) = x(2);
    dPhi(ii) = x(3);
    figure;
    plot(tau, Cknorm(:,k)','x')
    hold on;
    t = linspace(0,12);
    plot(t, C1(ii) + C2(ii)*cos(dPhi(ii)-t));
end;
```

Bibliography

[1] A. E. Kaplan and P. L. Shkolnikov, "Lasetron: A proposed source of powerful nuclear-time-scale electromagnetic bursts," *Physics Review Letters*, vol. 88, no. 7, p. 074801, 2002.

[2] L. da Silva, M. Perry, M. Felt, and B. Stuart, "The short pulse laser: A safe, painless surgical tool," *Science and Technology Review*, p. 29, 1995.

[3] M. Nakazawa, T. Yamamoto, and K. R. Tamura, "1.28 tbits/s-70km otdm transmission using third- and fourth-order simultaneous dispersion compensation with a phase modulator," *Electronics Letters*, vol. 36, no. 24, p. 2027, 2000.

[4] S. Bigo, Y. Fignac, G. Charlet, W. Idler, S. Borne, H. Gross, R. Dischler, W. Poehlmann, P. Tran, C. Simonneau, D. Bayart, G. Veith, A. Jourdan, and J.-P. Hamaide, "10.2 Tbit/s (256x42.7 Gbit/s PDM/WDM) transmission over 100 km TeraLight^{TM} fiber with 1.28 bit/s/Hz spectral efficiency," in *Optical Fiber Communication Conference and Exhibit, 2001*, vol. 4, 2001.

[5] K. Fukuchi, T. Kasamatsu, M. Morie, R. Ohhira, T. Ito, K. Sekiya, D. Ogasahara, and T. Ono, "10.92-tb/s (273 x 40-gb/s) triple-band/ultra-dense wdm optical-repeatered transimission experiment," in *Optical Fiber Communication Conference and Exhibit, 2001*, vol. 4, 2001.

[6] J. D. Moores, J. Korn, K. L. Hall, S. G. Finn, and K. A. Rauschenbach, "Ultrafast optical TDM networking: Extention to the wide area," *IEICE Transactions B: Commununications*, vol. E82-B, no. 2, p. 209, 1999.

[7] J. Debeau, B. Kowalski, and R. Boittin, "Simple method for the complete characterization of an optical pulse," *Optics Letters*, vol. 23, no. 22, p. 1784, 1998.

[8] R. Trebino, K. W. DeLong, D. N. Fittinghoff, J. N. Sweetser, M. A. Krumbrugel, B. A. Richman, and D. J. Kane, "Measuring ultrashort laser pulses in the time-frequency domain using frequency-resolved optical gating," *Review of Scientific Instruments*, vol. 68, no. 9, p. 3277, 1997.

[9] D. J. Kane and R. Trebino, "Characterization of arbitrary femtosecond pulses using frequency-resolved optical gating," *IEEE Journal of Quantum Electronics*, vol. 29, no. 2, p. 571, 1993.

[10] R. Trebino and D. J. Kane, "Using phase retrieval to measure the intensity and phase of ultrashort pulses: frequency-resolved optical gating," *Journal of the Optitcal Society of America A*, vol. 10, p. 1101, 1993.

[11] D. J. Kane and R. Trebino, "Single-shot measurement of the intensity and phase of an arbitrary ultrashort pulse by using frequency-resolved optical gating," *Optics Letters*, vol. 18, no. 10, p. 823, 1993.

[12] K. W. DeLong, R. Trebino, J. Hunter, and W. E. White, "Frequency-resolved optical gating with the use of second- harmonic generation," *Journal of the Optical Society of America B*, vol. 11, no. 11, p. 2206, 1994.

[13] D. N. Fittinghoff, K. W. DeLong, R. Trebino, and C. L. Ladera, "Noise sensitivity in frequency-resolved optical-gating measurements of ultrashort pulses," *Journal of the Optical Society of America B*, vol. 12, no. 1, p. 1955, 1995.

[14] E. P. Ippen, "Nonlinear optics course notes." course notes for 6.634 Nonlinear Optics at MIT, 2002.

[15] G. P. Agrawal, *Nonlinear Fiber Optics.* Academic Press, 2 ed., 1995.

[16] G. S. He and S. H. Liu, *Physics of Nonlinear Optics.* World Scientific, 1999.

[17] R. W. Boyd, *Nonlinear Optics.* Academic Press, 1992.

[18] D. Derickson, *Fiber Optic Test and Measurement.* Prentice Hall, 1998.

[19] Staff, *Diffraction Grating Handbook.* Bausch and Lomb Diffraction Grating Research Laboratory, 1970.

[20] E. B. Treacy, "Measurement and interpretation of dynamic spectrograms of picosecond light pulses," *Journal of Applied Physics*, vol. 42, p. 3848, 1971.

[21] J. L. A. Chilla and O. E. Martinez, "Direct determination of the amplitude and phase of femtosecond light pulses," *Optics Letters*, vol. 16, p. 39, 1991.

[22] K. W. DeLong, R. Trebino, and D. J. Kane, "Comparison of ultrashort-pulse frequency-resolved-optical-gating traces for three common beam geometries," *Journal of the Optical Society of America B*, vol. 11, no. 9, p. 1595, 1994.

[23] P. J. Delfyett, H. Shi, S. Gee, I. Nitta, J. C. Connolly, and G. A. Alphonse, "Joint time-frequency measurements of mode-locked semiconductor diode lasers and dynamics using frequency-resolved optical gating," *IEEE Journal of Quantum Electronics*, vol. 35, no. 4, p. 487, 1999.

[24] S. T. Cundiff, J. Ye, and J. L. Hall, "Optical frequency synthesis based on mode-locked lasers," *Review of Scientific Instruments*, vol. 72, no. 10, p. 3749, 2001.

[25] K. W. DeLong, D. N. Fittinghoff, R. Trebino, B. Kohler, and K. Wilson, "Pulse retrieval in frequency-resolved optical gating based on the method of generalized projections," *Optics Letters*, vol. 19, no. 24, p. 2152, 1994.

[26] K. W. DeLong and R. Trebino, "Improved ultrashort pulse-retrieval algorithm for frequency-resolved optical gating," *Journal of the Optical Society of America A*, vol. 11, no. 9, p. 2429, 1994.

[27] H. Stark, *Image Recovery: Theory and Application.* Academic, Orlando, 1987.

[28] J. R. Fienup, "Phase retrieval algorithms: a comparison," *Applied Optics*, vol. 21, no. 15, p. 2758, 1982.

[29] D. Peri, "Optical implementations of a phase retrieval algorithm," *Appl. Opt.*, vol. 26, no. 9, p. 1782, 1987.

[30] G. P. Agrawal, *Fiber-Optic Communication Systems.* John Wiley and Sons, 1992.